Dual-energy Stereoscopic X-ray Imaging to Enhance Soft-tissue Contrast in Lung Imaging

by

Wesley A. Bowman

Submitted in partial fulfilment of the requirements
for the degree of Master of Science

at

Dalhousie University
Halifax, Nova Scotia
July 2016

DEDICATION PAGE

I dedicate this thesis to my wife, Lydia. Without her, the completion of this work would not have been possible. Thank you for being you, and for supporting me through it all. I love you.

Table of Contents

LIST OF TABLES

LIST OF FIGURES

ABSTRACT

In this thesis, dual-energy x-ray technique is developed and discussed for a stereoscopic imaging system to enhance soft tissue contrast in lung imaging. The thesis starts with an introduction chapter on general physics of x-ray imaging, the dual energy technique, and image guided radiotherapy within a scope relevant to the thesis. The second chapter presents clinical data on lung stereotactic body radiation therapy (SBRT) to provide a motivation for dual-energy imaging for lung SBRT patients. In the third chapter, dual-energy x-ray imaging is developed by optimizing parameters for stereoscopic imaging system. The optimization is based on objective figures of merits to enhance soft tissue contrast and it utilizes both simulation and physical lung phantom data. Finally, a conclusion of the work is presented and multiple research avenues are discussed as potential future work of this thesis.

LIST OF ABBREVIATIONS USED

Z	Atomic number
HE	High-energy
LE	Low-energy
DE	Dual-energy
SE	Single-energy
ER	Energy ratio
DRR	Digitally reconstructed radiograph
CT	Computed tomography
CBCT	Cone-beam CT
ETX	ExacTrac x-ray
SBRT	Stereotactic body radiation therapy
MTF	Modulation transfer function
SLS	Simple log subtraction
ACNR	Anti-correlated noise reduction
EM	Electromagnetic
EBRT	External beam radiation therapy
IGRT	Image guided radiation therapy
GTV	Gross tumor volume
CTV	Clinical tumor volume
PTV	Planning target volume
ITV	Internal target volume
ETX	ExacTrac x-ray

SCLC	Small cell lung cancer
NSCLC	Non-small cell lung cancer
CDHA	Capital Health for Nova Scotia
SIFT	Scale invariant feature transform

ACKNOWLEDGEMENTS

First of all, I would like to thank my committee members and external reader, Dr. James Robar, Dr. Robin Kelly, Dr. Mike Sattarivand, and Dr. Chris Thomas, for their encouragement and knowledge that helped me through this journey. A special thanks to my supervisor Dr. Mike Sattarivand. Even though we had our differences, we never let that get in the way of getting work done. Dr. Sattarivand has been extremely timely in all things, which has really lead to a great conclusion of this work. Also, a thanks to Brainlab, AG for providing partial financial support for this research.

I would also like to thank my colleagues. I have learned numerous things from you, including skills not related to our field, but were nonetheless very interesting to me. You all have been a great source of friendship and entertainment. A special shout out to Tynan Stevens (Dr. Stevens), who allowed me to join him in a journey of hard work and creation.

As always, I have to thank my family. Without their love, support, and understanding, I would not be where I am today. I know the distance has been hard, but I thank you for supporting me in my life choices.

Finally, a massive thanks to my wife. Without you, this whole chapter of my life would have been entirely different, and I am sure that I would not be where I am without you. I cannot wait for the next chapter to begin, and I am thankful everyday that I can call you my wife. I love you.

CHAPTER 1: INTRODUCTION

Diagnostic imaging utilizes x-rays, which is a form of electromagnetic (EM) radiation, to image human body. Radio waves, visible light, x-rays and gamma rays are all different types of electromagnetic radiation. These different types of EM radiation are typically classified by their energy.

Electromagnetic radiation can be described in two ways, either as a wave or as a particle, which is known as the wave-particle duality. Discrete packets of EM energy are called photons. The energies of the photons are expressed in electron volts (eV). When the energy of the photon is greater than the binding energy of an electron, the photons have enough energy to ionize atoms by removing a bound electron from the atomic shell. Radiation in this range of energy is referred to as ionizing radiation. It takes 11.2 eV to ionize water, which is most often irradiated for medical imaging, since the human body is made of mostly water. Nonionizing radiation is any type of EM radiation that will not ionize an atom or molecule.

X-rays were discovered in 1895 by Wilhelm Roentgen [1]. Planar x-ray imaging is typically performed with x-rays going through the patient's body and being detected on with an x-ray detector that is outside the patient, as well as parallel and opposed to the x-ray source. The x-rays enter the patient and are attenuated by the different tissues inside of the patient. Different tissues have different attenuation properties based on their density and atomic number, and the x-rays that exit the patient are a heterogeneous distribution. The x-ray image is a picture of that heterogeneous x-ray distribution.

X-ray Production

When an electron's kinetic energy is converted into electromagnetic radiation, x-rays are produced. X-rays produced from the conversion of charged particle kinetic energy into photon energy is referred to as bremsstrahlung radiation, which is German for "breaking radiation."

An x-ray tube consists of an evacuated tube, a negatively charged metal filament called the cathode, and a positively charge metal anode. An illustration of an x-ray tube is shown in Figure 1.

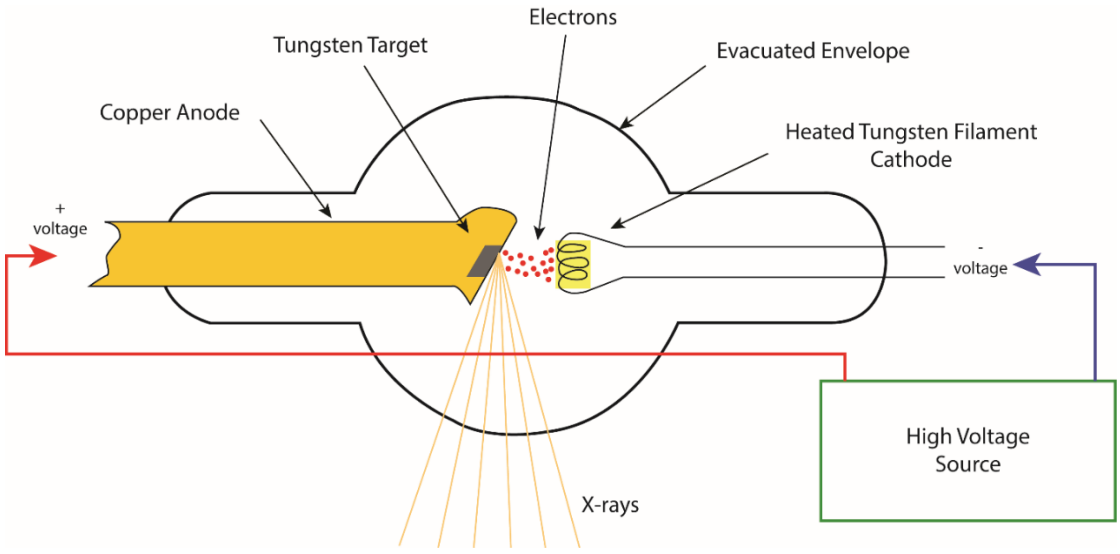

Figure 1 A x-ray schematic illustrating all the components of an x-ray tube [1].

When a current is passed through the cathode, electrical resistance increases the production of thermal electrons [1]. The electrons are then accelerated through a potential difference between the anode and the cathode. Thermionic emission occurs at very high temperatures, therefore the filament needs to be a metal with a high melting point, and

thus tungsten is used (3370°C melting point) [2]. The anode is positively charged, and serves as the target for the electrons released from the cathode. A potential difference is created between the anode and cathode, creating a negative charged anode and a positively charge cathode, which causes the electrons accelerate towards the anode. This potential difference is called tube voltage and is measured in volts (V). The kinetic energy gained by an electron is proportional to the voltage between the anode and cathode, e.g. 100 kV accelerates electrons to 100 keV. High energy electrons collide with the target atoms of the anode, and decelerate due to coulomb force interactions, which results in the production of bremsstrahlung radiation [1]. The probability that the electron will have a direct impact on the nucleus is very low, because most of the atom is empty space and the nuclear cross-section is small. This cross-section can be thought of as an effective target area, and for bremsstrahlung is proportional to Z^2. Therefore, lower energy x-rays are produced more often, and the number of higher-energy x-rays decreases approximately linearly with energy up to the maximum energy of the incident electrons. This ideal case of bremsstrahlung radiation happens when the beam is unfiltered. However, the beam will always be filtered by the x-ray target and the window of the x-ray tube. With filtration, the preferentially low energy x-rays are absorbed resulting in the mean energy of the x-ray spectrum to be about one-third of the highest x-ray energy in the spectrum. The distribution of x-ray energies for unfiltered and filtered bremsstrahlung spectra are illustrated in Figure 2.

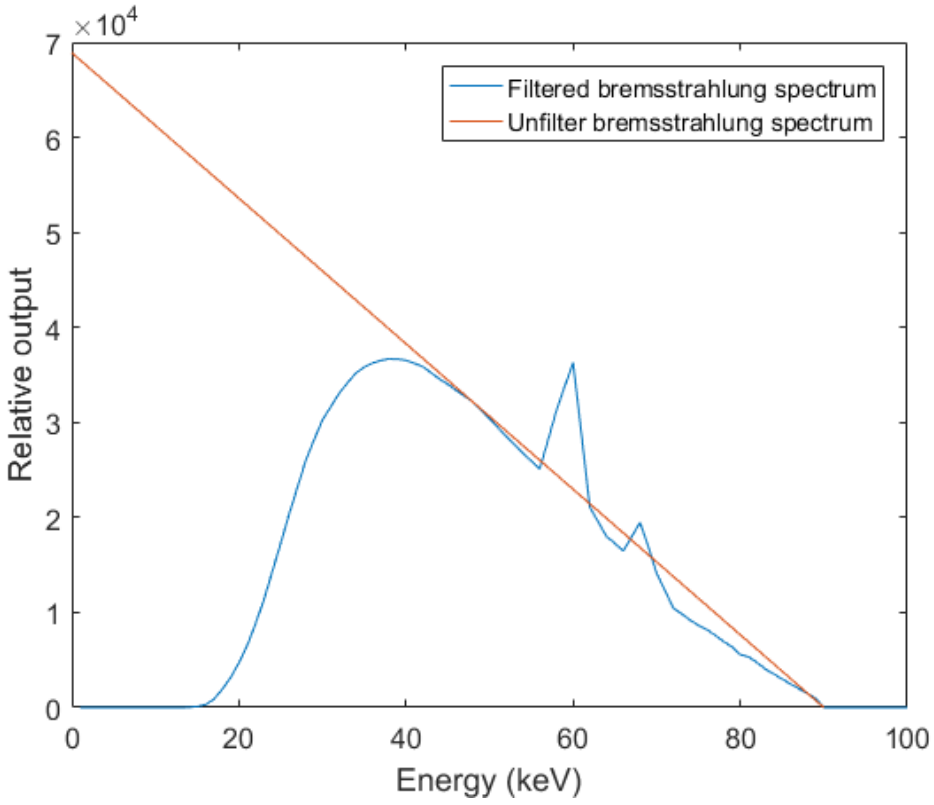

Figure 2 A typical bremsstrahlung distribution for a 90 kVp x-ray beam compared to an unfiltered bremsstrahlung distribution.

The two major factors on the efficiency of x-ray production are the kinetic energy in the incident electrons and the atomic number (Z) of the target in the anode. The approximate ratio of the radiative energy loss (i.e. bremsstrahlung radiation) to the collisional energy loss (heat loss) is [1]:

$$\frac{\text{Radiative Energy Loss}}{\text{Collisional Energy Loss}} = \frac{E_K Z}{820{,}000}$$

where E_K is the kinetic energy of the incident electron in keV, and Z is the atomic number of the target. Tungsten is a typical target since it has a high atomic number and high melting point. For a 120 keV electron impinging on a tungsten target (Z = 74), the ratio is 0.013 or 1.3%. Therefore, 98.7% of the kinetic energy is lost to heating, and only 1.3% of the electrons produce photons. This intense heating in the target can destroy the target over time, and a method to remove the excess heat is needed. To accomplish this a tungsten target is connected to a copper heat sink. Since copper has a higher specific heat capacity compared to tungsten, this allows the tungsten to transfer its heat into the copper, and the copper to dissipate the heat to the x-ray housing. The small area of the tungsten target still limits heat dissipation, and therefore a rotating anode is used. If the target is rotating, it limits the amount of time one particular spot of the target is getting bombarded. This allows for less degradation to the target, and better heat dissipation as well by spreading the thermal energy over a larger area of the target.

The anode, for diagnostic x-rays, is angled. This is primarily due to reduce the focal spot and to limit the self-attenuation of the photon beam due to the target. For low electron energies, bremsstrahlung photons are emitted isotropically. As the energy of the incident electrons increase, the angle narrows. This bremsstrahlung angular distribution is illustrated in Figure 3.

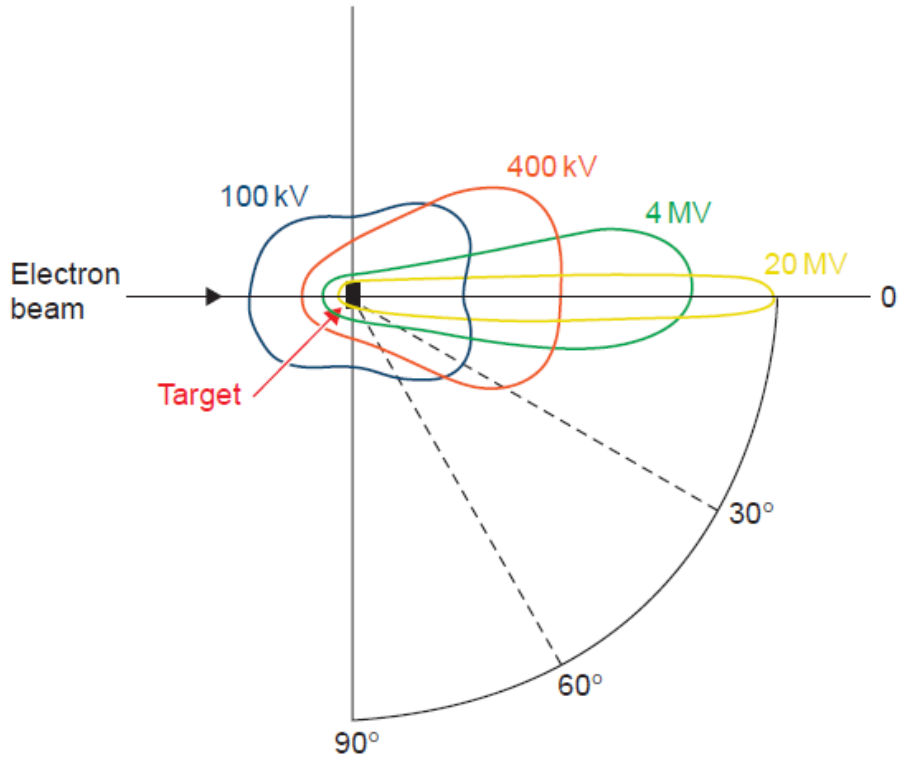

Figure 3 Relative intensity of bremsstrahlung radiated at various angles for electrons with KE of 100 keV up to 20 MeV [3].

The anode angle also affects the focal spot of the x-ray system. The focal spot size is defined in two ways, the actual spot size and the effective spot size. The actual spot size corresponds to the area of the anode that is bombarded with the electrons, and is primarily determined by the width of the cathode filament. The effective spot size is the length and width of the actual focal spot size as projected down the central axis in the x-ray field. The effective focal length is defined as

$$\text{Effective Focal Size} = \text{Actual Focal Size} \times \sin\theta$$

where θ is the anode angle. This is known as the line-focus principle. The anode angle is defined as the angle from the surface of the anode to the central ray in the x-ray field. Figure 4 illustrates the anode angle and the line-focus principle.

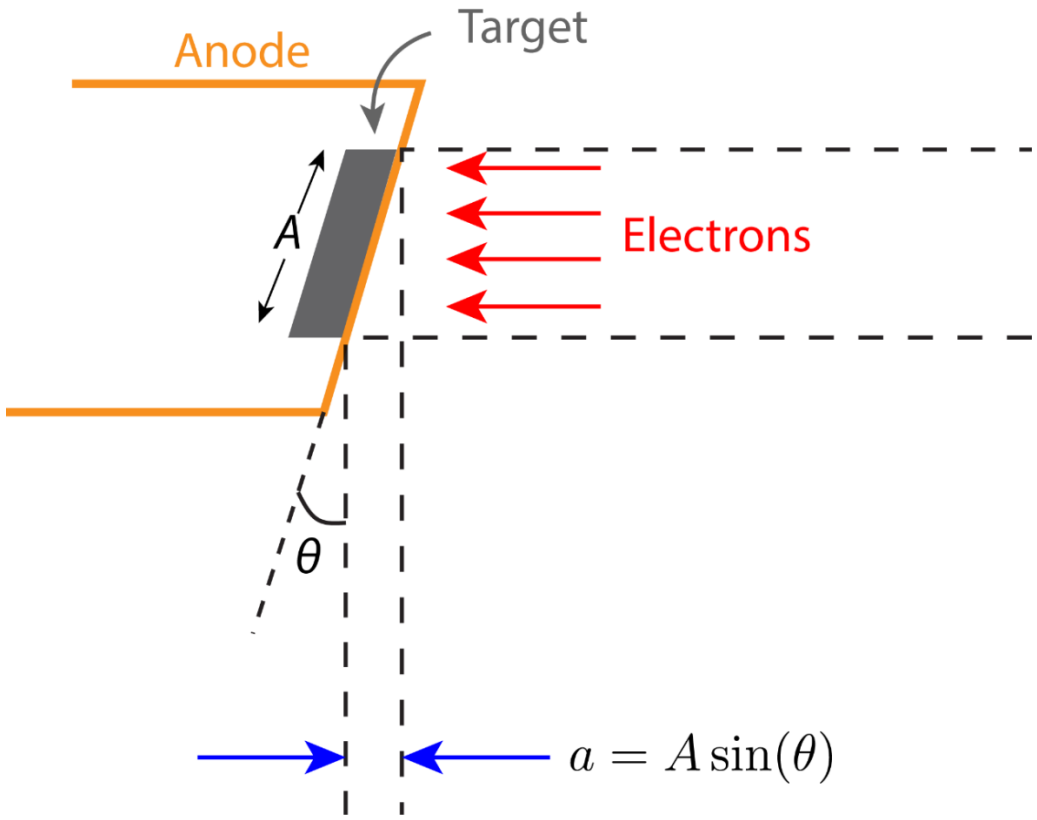

Figure 4 The anode angle and the line-focus principle illustrated with incident electrons coming from the right [1].

There are three major trade-offs to consider when considering a choice for the anode angle:

1. Field coverage
2. Effective focal spot size
3. Power loading

A small anode angle creates a smaller effective focal spot for the same actual focal area. A smaller effective focal spot provides higher spatial resolution, but can limit the field coverage. If one makes the actual focal spot smaller by decreasing the width of the focal size, then heating can become an issue because of the poor power loading. The most common anode angles are 12°-15° for general radiography with typical focal spots of 0.6 and 1.2 mm.

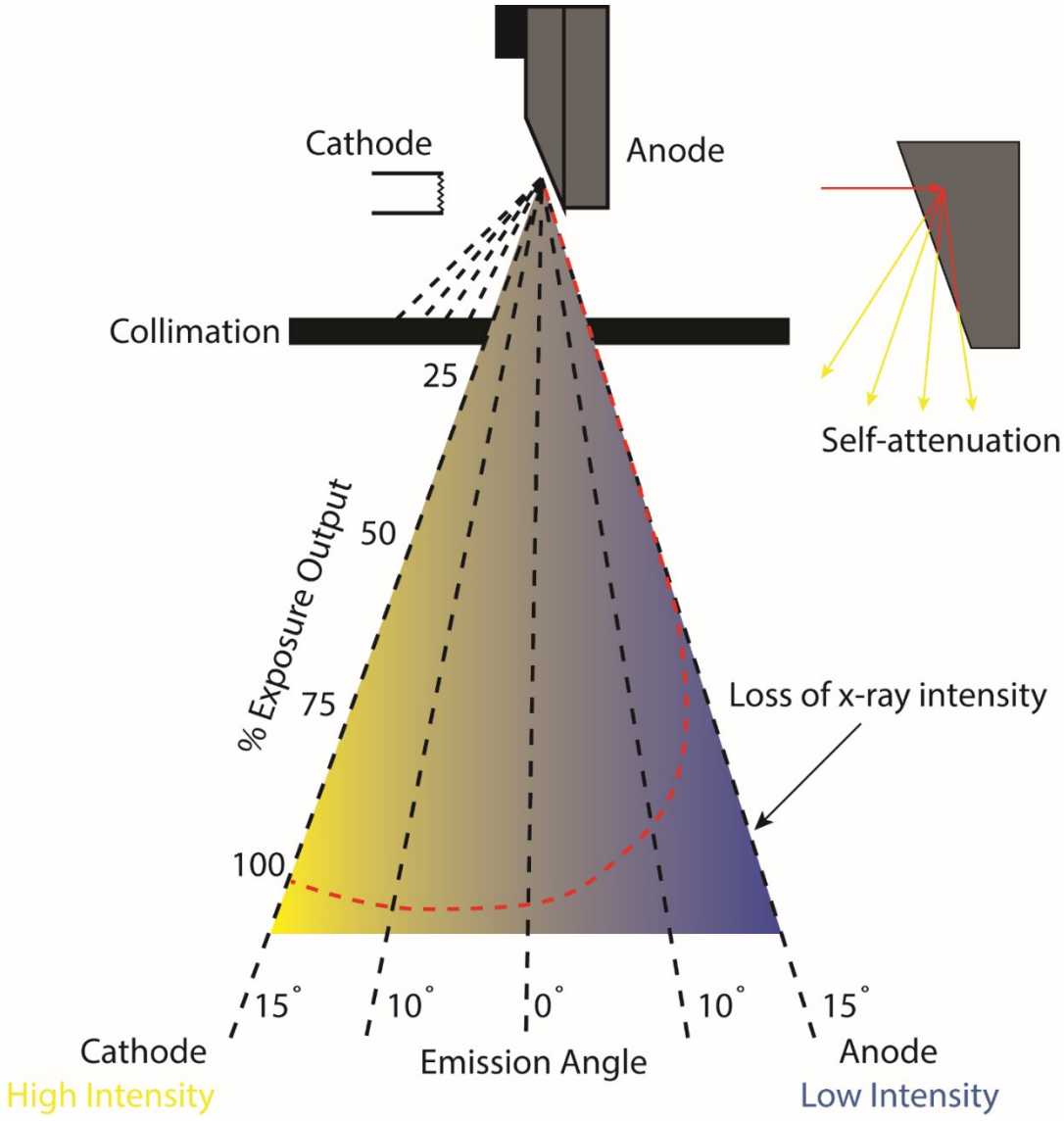

Figure 5 The heel effect illustrated with a graph of the exposure output vs emission angle [1].

X-rays are produced isotopically at depth in the target. However, since these x-rays are produced at depth in a high Z medium, most directions are highly attenuated. Photons that are in the thicker part of an angled target have to travel through a greater distance of the anode, and therefore experience more attenuation than those that are closer to the surface of the anode. This self-attenuation of the beam on the anode side (thicker side) is

referred to as the heel effect, and is illustrated in Figure 5. For larger source-to-image distance, the heel effect is less prominent because the heel effect occurs over a smaller distance. Since the cathode side of the field has greater beam intensity, the patient is typically positioned such that the cathode is oriented over the patient's thicker parts.

Photon Interaction with Matter

There are two major types of interactions of x-rays with matter in the diagnostic energy range, photoelectric absorption and Compton scattering. These types of interactions create ionizing radiation. The diagnostic energy range is from 20 kV to 150 kV. There is another interaction that creates ionizing radiation called pair production, however, it can only occur when the incident electron energy is higher than 1.02 MeV [1].

Photoelectric Effect

The photoelectric effect happens when an incident photon interacts with an orbital electron in an atom; all of the incident photon's energy is transferred to the electron which is ejected from the atom. The kinetic energy of the ejected electron (E_{pe}) is equal to the incident photon energy ($h\nu$) minus the binding energy of the orbital electron (E_b).

$$E_{pe} = h\nu - E_b$$

The binding energy is the energy required to remove an electron completely from the atom. For the photoelectric effect to occur, the incident photon energy has to be greater than the electron binding energy. Following a photoelectric interaction, the atom is ionized by the ejection of an inner-shell electron. In order to be in its lowest energy state, the atom fills this vacancy with an electron from a shell with a lower binding energy. The difference in the binding energy between these two states is released as a characteristic x-ray. A diagram of the photoelectric effect is shown in Figure 6.

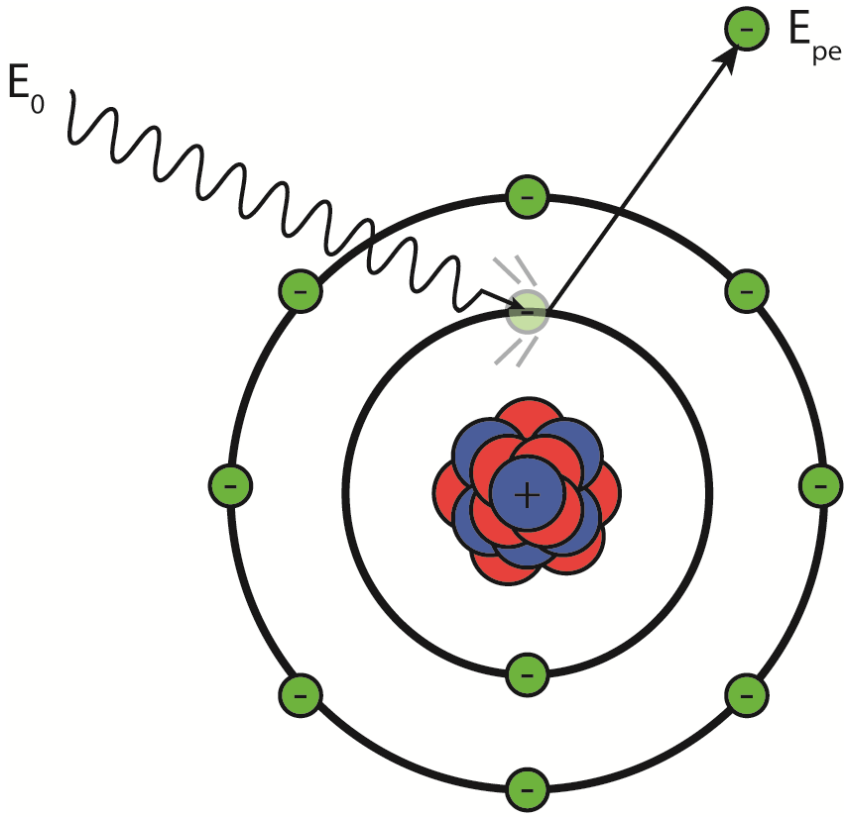

Figure 6 Photoelectric absorption is illustrated with characteristic x-rays being emitted after the electron cascades down [1].

The filling of a vacancy by an outer shell electron does not always result in the production of characteristic x-rays. The energy released can instead be transferred to an orbital electron which can escape the atom. This is known as an Auger electron. An illustrator of the characteristic x-ray and Auger electron process is presented in Figure 7.

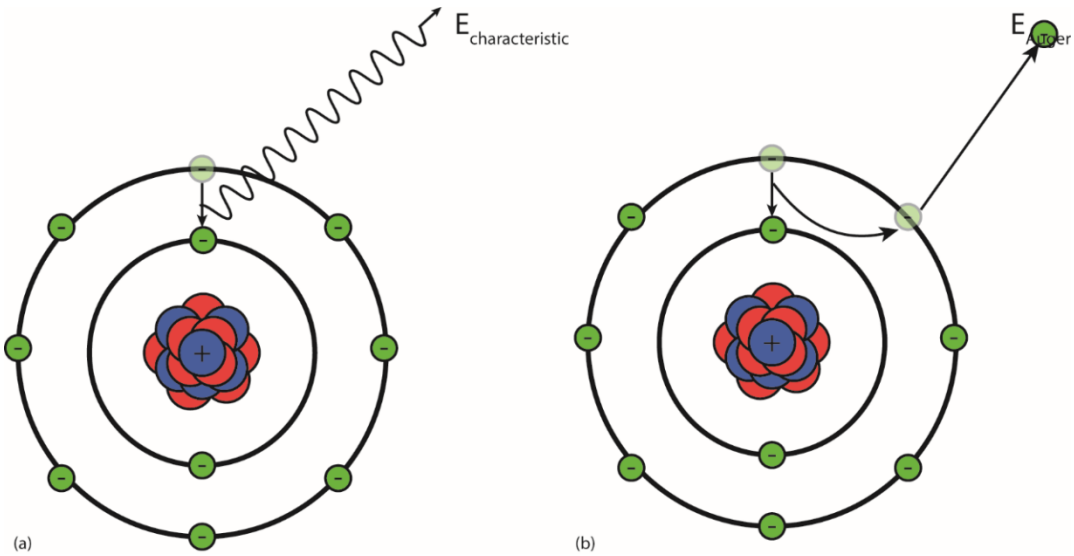

Figure 7 After a photoelectric interaction, an electron transitioning to fill the vacancy is either accompanied by (a) a characteristic x-ray, or (b) the emission of an Auger electron [1].

The probability of characteristic x-rays being emitted decreases as the atomic number of the material decreases. Therefore, at diagnostic energies, characteristic x-rays in soft-tissue are not typically detected since their energies are so low.

The probability of photoelectron absorption per unit mass is approximately proportional to Z^3/E^3, where Z is the atomic number and E is the energy of the incident photon [1]. This means that the probability of a photoelectric interaction in bone ($Z \approx 13.8$) is approximately 6.5 ($13.8^3/7.4^3$) times greater than in soft-tissue ($Z \approx 7.4$). However, the relationship is inversely proportional with respect to energy, i.e. if the photon energy is doubled, the probability of a photoelectric interaction is decreased by $1/2^3 = \frac{1}{8}$. However, this is only an approximation. Every element has absorption edges, where the probability of a photoelectric interaction is greatly increased. If a photons energy does not

exceed the electron's binding energy, the photoelectric effect cannot occur. Once an incident photon exceeds the binding energy of a bound electron, it can release that electron. This is when an absorption edge occurs, since when the photon exceeds that binding energy, the photoelectric effect can occur with that electron. These absorption edges are typically called by the name of the shell which the interaction is occurring in, such as K-edge or L-edge. The K-edge in tungsten is 69.5 keV.

The photoelectric effect dominates when lower energy photons interact with high Z materials. The photoelectric effect can be explored to amplify imaging signal differences between tissues and slightly higher atomic numbers due to Z^3 dependence. This is basis of contrast in diagnostic imaging.

Compton Scattering

Compton scattering occurs when a photon interacts with a free electron. The electron is ejected with a gained kinetic energy and a scattered photon is emitted with some reduction in energy relative to the incident photon. This interaction is most likely to occur with a valence electron, which tends to have a very low binding energy. Compton scattering is illustrated in Figure 8.

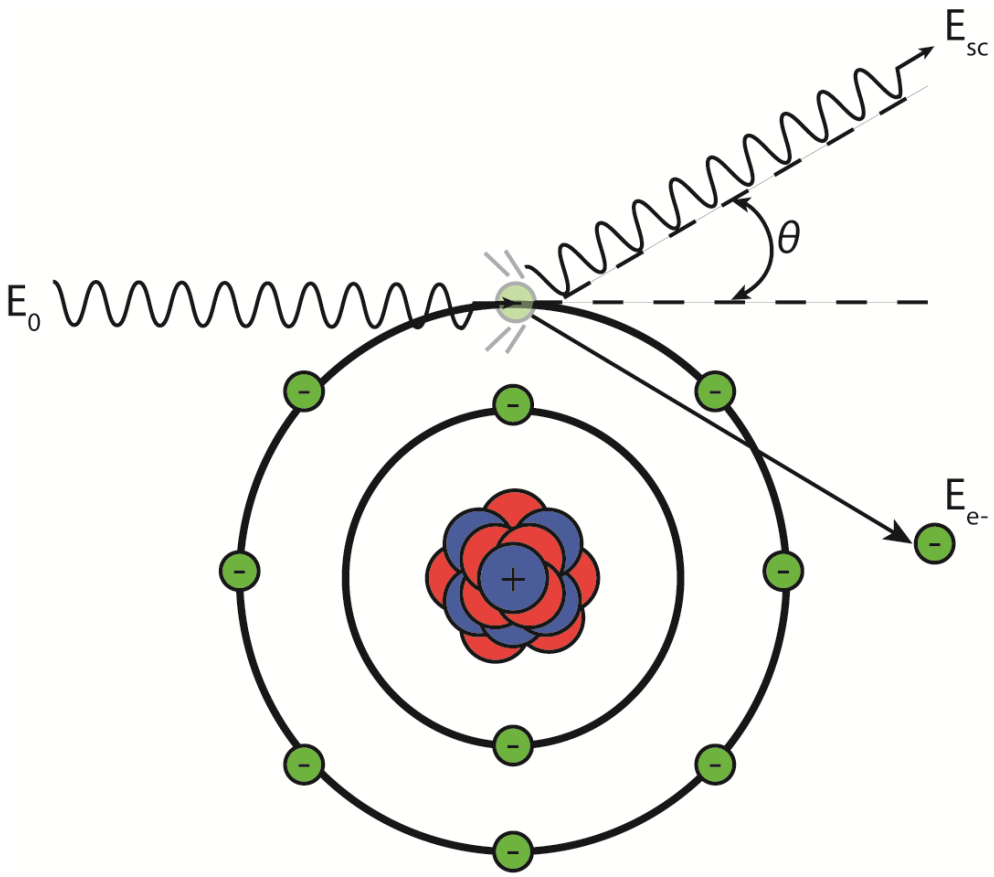

Figure 8 An incident photon interacts with a valence electron which results in the ejection of a Compton electron and a Compton scattered photon [1].

The energy of the scattered photon can be calculated by

$$E_{sc} = \frac{E_0}{1 + \frac{E_0}{m_e c^2}(1 - \cos\theta)}$$

where E_{sc} is the energy of the scattered photon, E_0 is the energy of the incident photon, m_e is the mass of the electron, c is the speed of light, and θ is the angle of the scattered photon (Figure 8) [1]. As the incident photons energy increases, both the scattered photon and electron are scattered more in a forward direction. For any given scattering angle, the

fraction of the energy transferred to the scattered photon decreases with increasing incident photon energy. The scattered electrons energy is calculated by

$$E_{e^-} = E_0 - E_{sc}$$

where E_{e^-} is the kinetic energy of the scattered electron. When Compton scattering occurs at the energies used in diagnostic imaging, most of the energy is transferred to the scattered photon. Usually, even at maximum energy loss, the scattered photons have a relatively high energy and tissue penetrability. If these scattered x-rays are detected, this results in a degradation of the image contrast and an increase in the random noise. The probability of Compton interaction is nearly proportional to the density of the material.

X-ray Detection

There are different types of photon detectors in diagnostic radiology. Below we describe screen-film and digital flat panel detectors.

Screen-film

In screen-film radiography, a sheet of film is placed between two intensifying screens. The screens and the film are placed inside of a light-tight case to prevent outside light interferes. The screen is made of a scintillator material that converts incident x-rays into visible light. The film consists of a base layer of thin plastic and is coated on one or both sides with an emulsion layer of silver halide (95% AgBr and 5% AgI) crystals held in a water-soluble gelatin. When the film is exposed to visible light, Ag^+ ions gain electrons and are converted into Ag, forming a latent image center. The screens and the film need to be close together to minimize the lateral spread of visible light produced by the screen, which causes image blurring. The intensifying screens are typically made with high Z materials to increase x-ray absorption efficiency. Thicker screens absorb more x-rays resulting in higher detection efficiency at the expense of lateral light spread. Therefore, there is a trade-off between detection efficiency and spatial resolution.

To produce an image, the film must be developed by placing the film in an aqueous solution containing a reducing agent, called the developer. The metallic silver elements, Ag, at the latent image centers act as a catalyst causing the remaining Ag^+ in that grain to be reduced. A grain of metallic silver atoms appears as a black speck on the film. After

passing through the developer, the film proceeds through another solution called the fixer that dissolves the remaining silver halide emulsion that was not exposed. The film is then rinsed with water to remove any residual developer or fixer and then dried. Since the metallic silver appears as a black speck on the film, x-ray films are negatives, i.e. a higher exposure produces a darker image. Therefore, a gray scale image is produced from the x-rays that is darker where there is less attenuation (e.g. lung) and lighter where there is more attenuation (e.g. bone).

Intensifying screens respond linearly to incident x-ray exposure, so twice as much exposure means twice as much visible light is produced. The film emulsion, however, has a non-linear response for a screen-film system. An H and D curve (Hurter and Driffield) is a plot of the optical density (OD) of the processed film verses the log of the relative exposure. Optical density is defined as

$$OD = -\log_{10}(T)$$

where T is the transmittance of the film defined as,

$$T = \frac{I}{I_0}$$

where I is the intensity of the light transmitted through the film, and I_0 is the intensity of the light source at the same point without the film. The human eye responds approximately logarithmically to light intensity, and therefore an OD of 1 appears twice as bright as an OD of 2 [1]. An example H and D curve is shown in Figure 9.

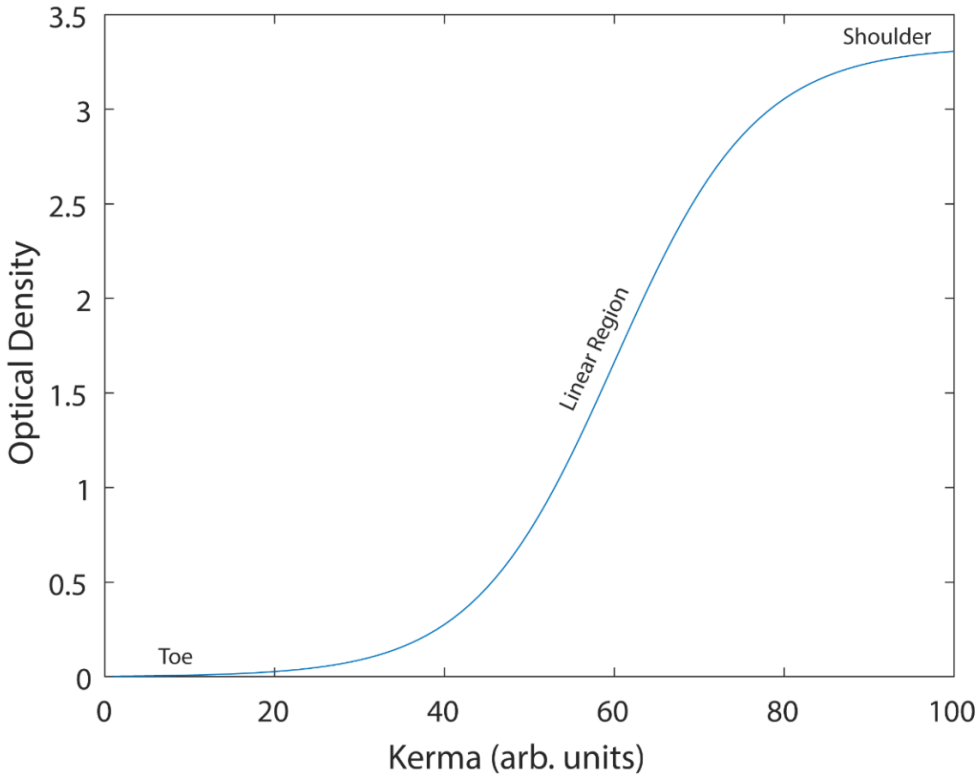

Figure 9 An H and D curve showing the different regions of the curve [1].

Films can be more sensitive, have different levels of contrast, and different dynamic ranges. The sensitivity of a film (film speed), refers to the amount of exposure needed to produce a given OD. This can be noted as a horizontal shift in the H and D curve. The contrast of a film is related to the slope of the H and D curve. Contrast can be improved by increasing the slope of the linear region, at the expense of reducing the dynamic range (film latitude), which is the lateral width of the slope in the linear region. These concepts are illustrated in Figure 10.

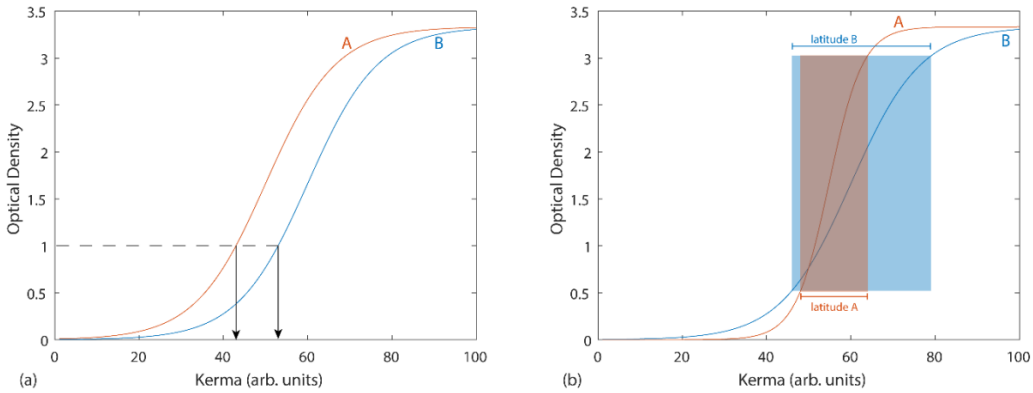

Figure 10 An H and D curve illustrating the different characteristic regions of the curve. (a)presents the different speeds of two curves, while (b) displays two curves with different contrast and latitude [1].

High contrast films are not suitable for all applications. There are instances where a higher latitude is needed, such as in chest radiography. This is due to presence of both highly attenuating mediastinum and the highly transmissive lung tissue.

Digital Flat Panel Detectors

Flat panel thin-film-transistors (TFT) array detectors are made of amorphous silicon that read out charge from individual detector elements called dexels. Each dexel has a light sensitive area and a light-insensitive area where the electronic components are located. The fill factor is the percentage of the dexel that is photosensitive which places a limitation to how small a dexel can be.

TFT arrays are employed in two types of flat panel detectors: indirect and direct. The indirect detectors use a scintillator to convert the x-rays to visible light and then a

photodiode to capture the visible light and produce charge that is read by the TFT array. Certain scintillators can be grown in columnar crystals, which act as a pipe for the visible light. These light pipes help reduce the lateral spread of the light, thus preserving spatial resolution. A typical scintillator with light pipes is cesium iodine (CsI).

The direct x-ray conversion detectors use a semiconductor material that makes use of electron-hole pairs that are proportional to the incident x-ray intensity. Absorbed x-ray energy is directly converted into charge in the detector. Amorphous selenium (a-Se) is the semiconductor most widely used. The a-Se is layered between two surface-area electrodes. Ion pairs are collected under applied voltage across the electrodes. The electric field prevents lateral spread of the charge in the semiconductor, resulting in a high spatial resolution. Due to its low atomic number, the selenium layer has to be thick to improve detection efficiency. Figure 11 illustrates the difference between indirect and direct detection.

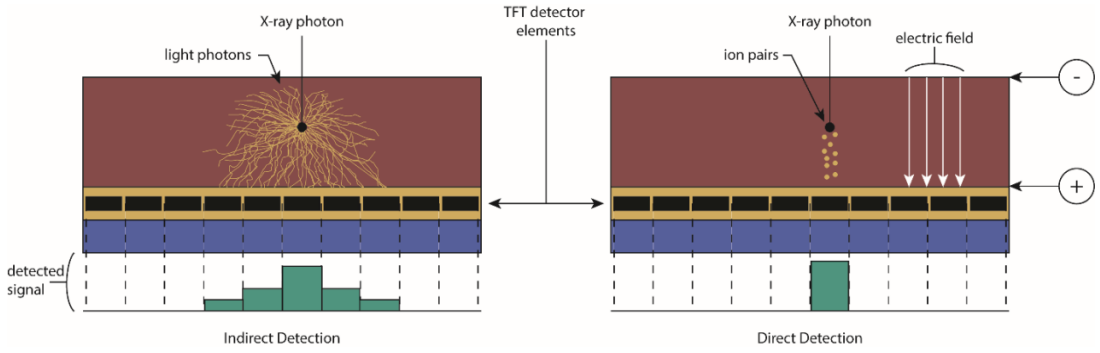

Figure 11 Indirect vs direct conversion of x-rays shown for TFT arrays [1].

Digital flat panel detectors have several advantages over the conventional screen-film detectors. In the screen-film radiography, the film OD dictates the required exposure to the user. A given screen-film has a fixed speed, and if an image is over or underexposed, the image has to be re-exposed. Digital detectors have wider latitude and a variable speed. With this wider dynamic range, digital detectors are more forgiving for an over- or underexposed image. Digital images can conveniently be stored in a computer and be assessed and shared at a later time for processing or follow up. Digital images also bypass the need for any chemical processing, which increases the time and cost efficiency. The images are also available for immediate previewing.

Dual-Energy Imaging

Dual-energy (DE) imaging takes advantage of the linear attenuation coefficients of different materials. The linear attenuation coefficient (μ) is the fraction of photons removed from a monoenergetic beam of x-rays per unit thickness of the material and is expressed in units of inverse centimeters (cm^{-1}) [1]. The linear attenuation coefficient has a non-linear relationship with energy and is a summation of individual linear attenuation coefficients from the different types of interaction:

$$\mu = \mu_{Rayleigh} + \mu_{photoelectric} + \mu_{Compton} + \mu_{pair\ production}$$

For the energy range of photons used in diagnostic images, the linear attenuation coefficients decrease with increasing energy, except at the absorption edges (typically only K-edges exist in the diagnostic energy range).

Not only will the energy affect the amount of interactions, but the density of a given material will as well. As the number of atoms per unit volume increase, there is linearly a higher probability of an interaction. The linear attenuation coefficient is often normalized to unit density and is called the mass attenuation coefficient (μ/ρ), in units of cm^2/g. Figure 12 illustrates the summation of different x-ray interaction's mass attenuation coefficients as well as the overall mass attenuation coefficient for soft-tissue. The data for this plot is from National Institute of Standards and Technology (www.nist.gov) XCOM photon cross-sections database.

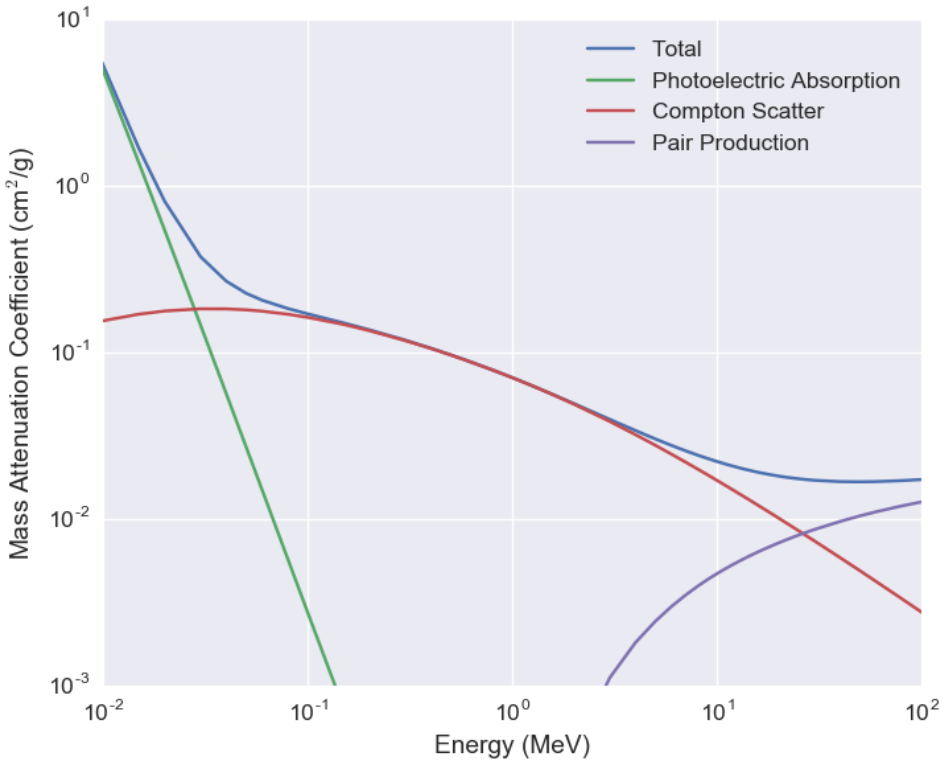

Figure 12 A plot of the different mass attenuation coefficients for soft-tissue, illustrating how the different x-ray interactions combine to form the overall mass attenuation coefficient.

The exponential relationship between the incident number of photons (N_0), and the transmitted photons (N) is described by Beer's law:

$$N = N_0 e^{-\mu x}$$

where x is the thickness of the material. The same relationship exists for beam intensity (i.e. number of photos per unit area):

$$I = I_0 e^{-\mu \cdot x}$$

where I is the exiting intensity, I_0 is the incident intensity. For two different materials, the equation becomes:

$$I = I_0 e^{-\mu_1 x_1} e^{-\mu_2 x_2} = I_0 e^{-\mu_1 x_1 - \mu_2 x_2}$$

DE utilizes the difference in atomic number for two materials and their energy dependence, i.e. bone and soft-tissue. The effective atomic number (Z_{eff}) for bone and soft-tissue is approximately 13.8 and 7.4 [3].

The mass attenuation coefficients of bone and soft-tissue are plotted in Figure 13. The data for this plot is from National Institute of Standards and Technology (www.nist.gov).

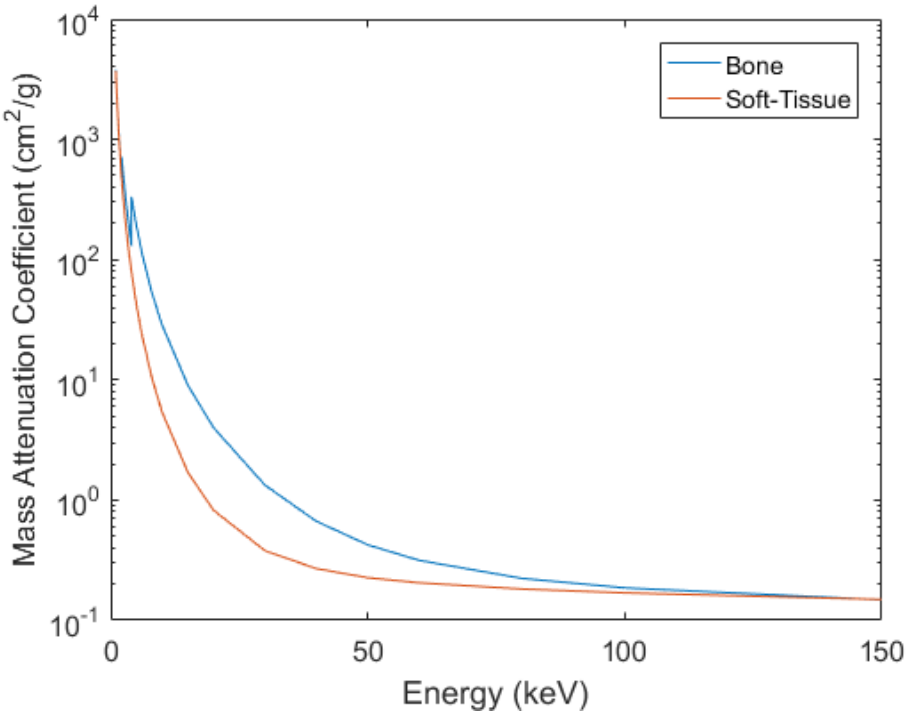

Figure 13 A plot of the different mass attenuation coefficients for soft-tissue and bone showing their energy dependence.

The energy dependence results in the separation between the mass attenuation coefficients. For bone, there is a higher probability of a photoelectric interaction, since the photoelectric interaction probability is proportional to Z^3/E^3. As the energy increases, the two materials become less separated as the Compton interaction starts to become dominate. Due to this energy dependence in different tissue types, the acquisition of two different energy images (using two different tube potentials), enables the bone or soft-tissue component of the images to be removed by post image processing. The simplest method to achieve a dual-energy image is to perform a simple log subtraction (SLS).

$$\log(I_{DE}) = \log(I_{HE}) - w\log(I_{LE})$$

A log subtraction is based on manipulating Beer's law.

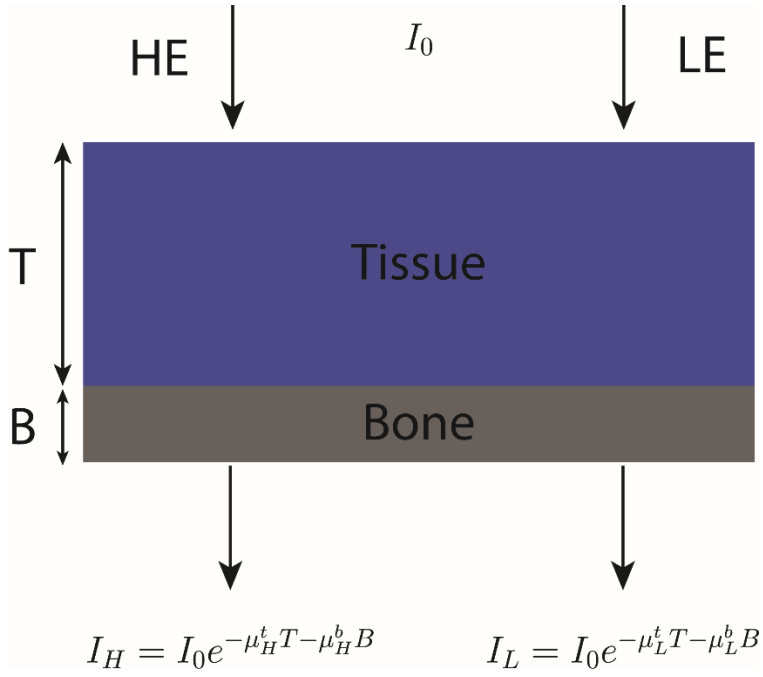

Figure 14 An illustration of Beer's Law for two different energies.

If two images are acquired at two different monoenergetic energy x-rays (H for high and L for low) passing through two different materials, bone (B) and soft-tissue (S), then we have:

$$I_L = I_{0,L} e^{-\mu_{B,L} x_B - \mu_{S,L} x_S}$$

$$I_H = I_{0,H} e^{-\mu_{B,H} x_B - \mu_{S,H} x_S}$$

where I_L and I_H are for LE and HE exposures, respectively. A simplified example is illustrated in Figure 14. Here, $\mu_{B,L}$ and $\mu_{S,L}$ are the linear attenuation of bone and soft-tissue for LE, $\mu_{B,H}$ and $\mu_{S,H}$ are the linear attenuation of bone and soft-tissue for HE, x_B

and x_S is the thickness of bone and soft-tissue, and I_L and I_H represent the low and high energy images respectively.

Taking the log of both sides of the equations:

$$\log(I_L) = \log\left(I_{0,L} \cdot e^{-\mu_{B,L}x_B - \mu_{S,L}x_S}\right) = \log(I_{0,L}) - \mu_{B,L}x_B - \mu_{S,L}x_S$$

$$\log(I_H) = \log\left(I_{0,H} \cdot e^{-\mu_{B,H}x_B - \mu_{S,H}x_S}\right) = \log(I_{0,H}) - \mu_{B,H}x_B - \mu_{S,H}x_S$$

Since these equations are linear, one of the materials can be cancelled out by a weighting factor subtraction [4].

$$\log(I_{DE}) = \log(I_{HE}) - w\log(I_{LE})$$

$$\log(I_{DE}) = \left[\log(I_{0,H}) - \mu_{B,H}x_B - \mu_{S,H}x_S\right] - w\left[\log(I_{0,L}) - \mu_{B,L}x_B - \mu_{S,L}x_S\right]$$

$$\log(I_{DE}) = \log(I_{0,H}) - \mu_{B,H}x_B - \mu_{S,H}x_S - w\log(I_{0,L}) + w\mu_{B,L}x_B + w\mu_{S,L}x_S$$

If we intend to cancel out bone, then we would set the bone components to 0 and solve for w,

$$0 = -\mu_{B,H}x_B + w\mu_{B,L}x_B$$

$$w_B = \frac{\mu_{B,H}x_B}{\mu_{B,L}x_B} = \frac{\mu_{B,H}}{\mu_{B,L}}$$

The same process can be performed to eliminate the soft-tissue,

$$0 = -\mu_{S,H}x_S + w\mu_{S,L}x_S$$

$$w_S = \frac{\mu_{S,H}x_S}{\mu_{S,L}x_S} = \frac{\mu_{S,H}}{\mu_{S,L}}$$

Simple log subtraction is written as

$$\log(I_{SLS}) = \log(I_{HE}) - w\log(I_{LE})$$

for soft-tissue only DE images, and as

$$\log(I_{SLS}) = -\log(I_{HE}) + w\log(I_{LE})$$

for bone-only DE images.

A more complex DE image algorithm can be implemented for noise reduction in the post image processing. Subtracting the high and low exposure images, inherently amplifies noise in the resultant DE image. To reduce noise amplification during DE subtraction, an anti-correlated noise reduction (ACNR) algorithm [5] [6] [7] could be used. For soft tissue DE imaging, ACNR algorithm significantly suppresses noise with minimal loss in spatial resolution as measured by the modulation transfer function (MTF) [8]. The soft-tissue image using ACNR is

$$\log(I_{ACNR}) = \log(I_{SLS}) + w_n\log(I^c_{SLS}) * h_{HPF}$$

where

$$\log(I^c_{SLS}) = w_c\log(I_{LE}) - \log(I_{HE})$$

is the complimentary image (i.e. the bone only SLS image), w_c is the tissue cancellation parameter for the complimentary image, h_{HPF} is a high-pass filter, w_n is a relative weighting factor, and $*$ indicates the convolution operation [8].

Radiotherapy

So far we focused on the use of x-ray in the context of diagnostic imaging which is in the kV energy range. However, x-rays can also be used in the MV range for cancer treatment by killing malignant cells, a concept referred as radiotherapy. In conventional external beam radiotherapy (EBRT), a typical fractionation scheme is 35 fractions, each delivering approximately 2 Gy of radiation dose per fraction [9]. However, stereotactic body radiation therapy (SBRT) is a highly conformal radiation dose that is delivered in large doses over several small fractions (hypofractionated) to an extra-cranial tumor target volume. This dose typically has a sharp falloff outside of the tumor region to spare normal organs at risk. This type of radiation therapy is preferred since it delivers an ablative dose to the tumor, but spares all the normal tissue in the neighboring regions [10].

The radiobiology of this type of radiotherapy can be thought of in terms of the normal tissue cell function. Each set of normal tissue is composed of working cells that have a particular function. Lung cells are specialized for the lung, and likewise for liver cells. Each region of normal tissue has a large population of these very specialized cells, and they also have some clonogenic cells that can replenish those specialized cells when they die. If the lung is exposed to radiation below a certain threshold, the clonogenic cells can potentially repair the damage that the radiation caused to those specialized cells. However, if the dose is above that threshold, then all the clonogenic cells within that region will also die, negating the possibility to repair and the region will lose its function.

Since these regions are very specialized, cells from other areas cannot come in to lend a hand at the repairs. Additional dose beyond the threshold does not increase the amount of volume affected. With this model of radiobiology in mind, one can imagine delivering an ablative dose to a single region that has a sharp falloff so that the other specialized cells around that region stay alive. This ensures that the region as a whole can still perform its specialized functions, while killing certain tumor regions, which is intended to be killed. It is very crucial not to kill off more than a certain volume of the spared organ, such that the basic organ function can still be sustained after radiotherapy [10]. Another reason that SBRT might be preferred over conventional radiotherapy is that it is a hypofractionation scheme. In conventional radiotherapy, the dose is given over a large number of fractions. This is to help the normal tissue repair from any damage it might be receiving from the radiation. By delivering more dose in less fractions, it is limiting the amount of repair that can happen, since the dose is above the threshold for cell death. This is why it is very important that the dose be highly conformal to the tumor volume [10].

SBRT has increased treatments times, and these longer treatment times provide more likelihood for motion to occur during the treatment (intrafraction motion). To reduce the damage to surrounding tissues, or the organs-at-risk (OARs), the patient is typically immobilized to improve the accuracy of the dose delivery. Otherwise, if the patient moves during treatment, then high radiation dose may be delivered to the nearby organs, negating what is aimed to be avoided in SBRT. However, immobilization can be difficult, especially if respiratory motion is involved, such as the case for lung SBRT. This respiratory motion has to be accounted for. There are three main categories for motion control: motion dampening, motion gating, and motion tracking [11]. Motion dampening

includes abdominal compression and breath holding. In the motion gating approach, the radiation beam is only activated for a certain phase of the breathing cycle. In the motion tracking technique, the tumor is tracked while the beam is on. This is usually performed with fiducials (i.e. a radiopaque object) implanted in the tumor volume. For treatment planning to incorporating motion management, a four-dimensional (4D) CT is used to determine the tumor motion during the breathing cycle. Typically, in a patient's plan, there is a gross target volume (GTV), a clinical target volume (CTV), an internal target volume (ITV), and a planning target volume (PTV). The GTV is the tumor that is palpable or can be identified radiographically. The CTV includes GTV plus a margin to account for any microscopic disease outside GTV. The ITV is used when tumor motion needs to be accounted for and includes all CTVs in different phases of breathing cycle. The PTV includes the ITV (or CTV if no motion management is used) plus a setup margin due to the uncertainties in patient setup and treatment delivery [3]. SBRT aims to deliver very conformal dose to PTV. Steep dose falloff outside of the PTV is also desired, to minimized damage to the surrounding normal tissues.

Different devices may be used for SBRT such as TrueBeam STx platform, which is a high-precision linear accelerator (linac) from Varian (Varian Medical Systems, Inc., Palo Alto, CA, USA) capable of image guided radiation therapy (IGRT). IGRT is an essential requirement for SBRT which can be achieved by the On-Board Imager (OBI) device on the Varian linac. OBI consists of a gantry mounted x-ray tube and a flat panel detector allowing acquisition of cone beam computed tomography (CBCT) data for image guidance (Figure 15). An in-room mounted imaging system can also be used for image guidance such as Brainlab ExacTrac stereoscopic image-guidance system (Figure 15).

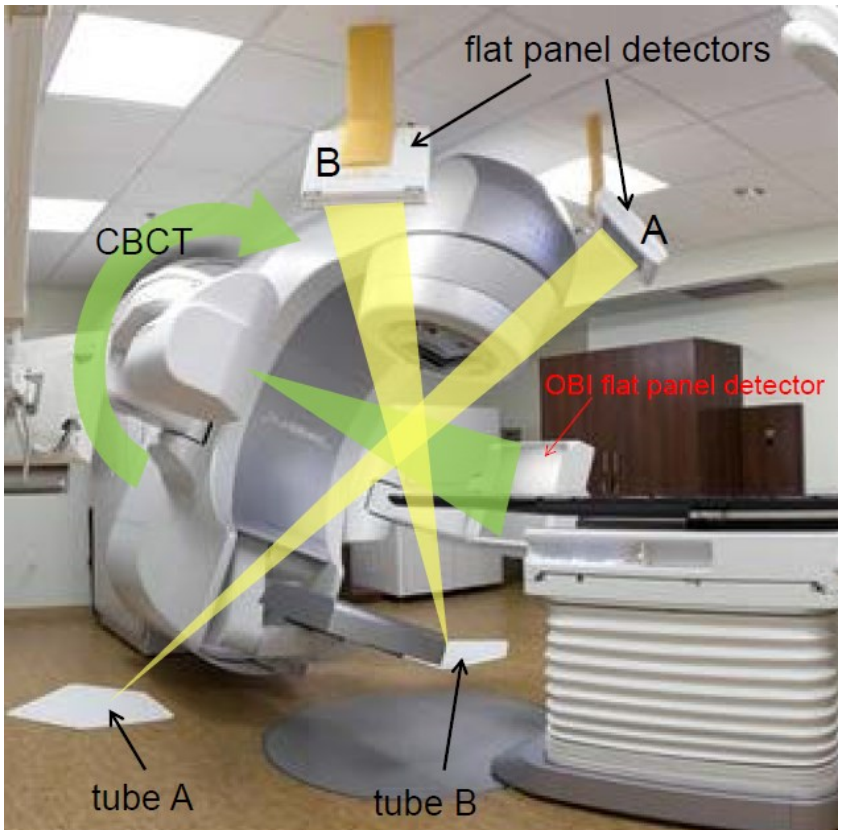

Figure 15 An illustration of the both the tubes from the ExacTrac x-ray system, the flat panel detectors, and the OBI.

The ExacTrac X-ray (ETX) system consists of a pair of floor mounted x-ray tubes and ceiling mounted flat panel detectors. These x-ray tubes are at oblique angles relative to the patient, and so the image axes do not correspond to the orthogonal axes of the treatment room. To align the patient in the treatment position, the x-ray images acquired with the ETX are compared to digitally reconstructed radiographs (DRRs) from treatment planning CT. DRRs are simulated planar images that are reconstructed from the planning CT dataset. DRRs are created by using a ray tracing algorithm by using the information

within the voxel of the CT dataset. This is essentially using Beer's law to calculated the attenuation through a line integral. In this case, the DRRs are projected onto the same oblique angles of ETX with respect to the patient.

CHAPTER 2: CLINICAL MOTIVATION TO DEVELOP DUAL-ENERGY X-RAY SYSTEM FOR STEREOSCOPIC IMAGING

SBRT for Lung Cancer

Lung cancer is the leading cause for cancer death in men, and the second leading cause for cancer death in women [12]. It accounted for approximately 27% of cancer deaths in the United States in 2014, and it was estimated that lung cancer accounted for 19% of all cancer deaths worldwide in 2012 [12]. Approximately 1 in 14 males, and 1 in 17 females will develop lung cancer in their lifetime [13]. It is estimated that there will be approximately 225,000 new cases of lung cancer and 158,000 deaths from it in 2016 in the United States alone. A major risk factor for increases the chances of developing lung cancer is smoking. Smoking is attributed to 80 to 90% of all lung cancers [12]. Other risk factors include radon, asbestos, air pollution, and ionizing radiation.

There are two main types of lung cancer: small cell lung cancer (SCLC) and non-small cell lung cancer (NSCLC). Approximately 80-85% of lung cancer is NSCLC, while about 10-15% is SCLC. SBRT is the standard of care for early stage (stage I and IIa) non-operative NSCLC [12] which accounts a large number of patients. This highlights the importance of SBRT in treating lung cancer patients.

Image Guidance for Lung SBRT

SBRT delivers large amounts of radiation dose to the tumor in limited number of fractions. As such, accuracy in patient alignment in SBRT is a fundamental requirement.

This can be achieved using either an in-room mounted stereoscopic imaging system or a linac gantry mounted CBCT system.

The x-ray tubes and detectors from the ETX stereoscopic system are mounted in a fixed geometry inside the room. Image acquisition does not involve treatment interruption, and thus it can image the patient at any time to verify the patient's positioning provided that the imaging view is not blocked by the linac gantry. However, the ETX provides projection images, which has limited contrast and only provides a 2D view of the patient.

Volumetric 3D images can be acquired though CBCT of the patient. However, CBCT requires a long acquisition time, and is therefore more prone to anatomical motion and blurring. CBCT also delivers more imaging dose to the patient compared to EXT, and it cannot be used while the treatment is in progress.

NSHA Experience in Treating Lung SBRT Patients

SBRT program in NSHA (Nova Scotia Health Authority) started in 2013 with treating lung as the first site. The clinic's treatment room is equipped with a OBI image guidance capable of CBCT imaging on a Varian TrueBeam platform as well as an in room mounted ExacTrac stereoscopic imaging system with a robotic treatment couch. The

couch is capable of aligning the patient in 6 degrees of freedom (6D), i.e. 3 translations and 3 rotations (Figure 16).

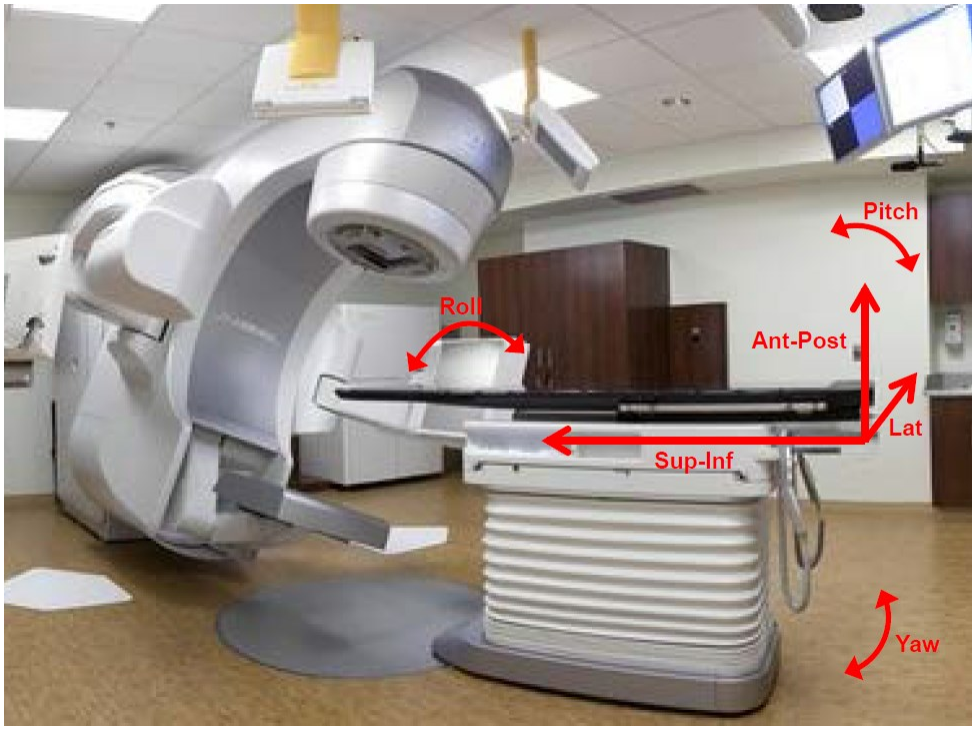

Figure 16 Varian couch with BrainLab couch top capable of patient alignment in 6 degrees of freedom.

In our clinic, the typical workflow of a patient is illustrated in Figure 17. Following a CT-simulator scan, the patient's plan is created based on clinical lung SBRT protocol. Once the patient is on the treatment couch, the ExacTrac x-ray system is used to align the patient by matching the stereoscopic images to the corresponding DRRs. Since the ExacTrac stereoscopic system is a projection imaging method, often the tumor is not visible due to low contrast or it may be overlapped by a rib bone. Therefore, matching relies on imaging sufficient, distinct bony anatomy, and the spine is used as a surrogate

for patient alignment. The spine, however, is not often visible in stereoscopic images of the lung, and thus a virtual isocenter is placed on the patient's spine in the treatment planning software. Hence, the couch is shifted to this virtual isocenter to acquire stereoscopic images and apply the patient alignment in 6D (Figure 17), and then the couch shifted back to the treatment isocenter. After the ExacTrac system alignment, a CBCT is acquired to verify the correct patient alignment based on soft-tissue matching as the tumor is visible on CBCT. The matching is performed around the PTV volume plus a 5 mm margin around it, and this volume is matched to the corresponding volume from planning CT. If the CBCT matching is within a specified tolerance (typically 3 mm shift and 3° rotation), the patient is ready for treatment. Otherwise, the patient will be aligned based on CBCT before initiating the treatment.

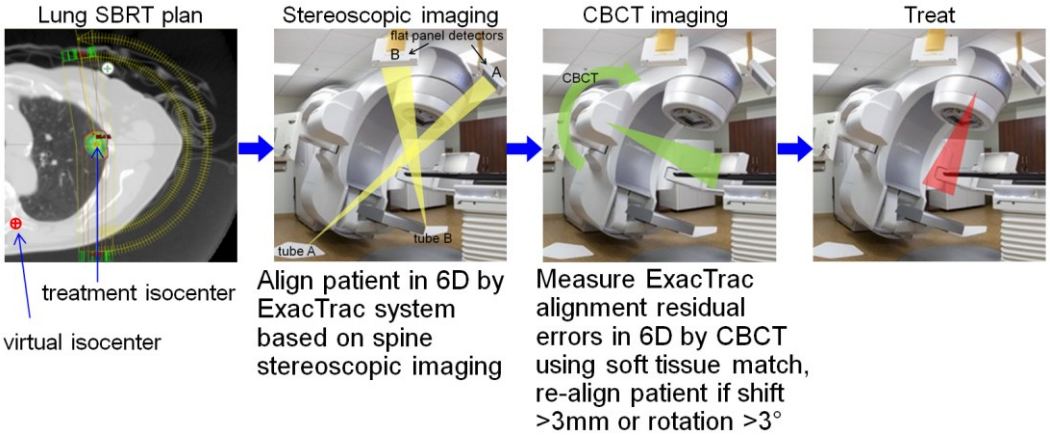

Figure 17 The lung SBRT patient workflow used in our clinic.

Is Stereoscopic Image Guidance using Spine Surrogate Valid to Align Lung SBRT Patients?

The content of this chapter is based on the following work which was presented at COMP 2016 annual meeting: Clinical assessment of ExacTrac stereoscopic imaging of spine alignment for lung SBRT, Mike Sattarivand, Clare Summers, and James Robar

The above lung SBRT patient workflow is designed to utilize the stereoscopic imaging system before CBCT. As noted above, the stereoscopic alignment is much faster than the CBCT with much less imaging dose. However, as stereoscopic system uses spine as surrogate for lung tumor alignment, its validity needs to be evaluated. Having CBCT data following the stereoscopic imaging for all the lung SBRT patients in CDHA, a small retrospective study was performed to evaluate the validity of spine matching to align lung SBRT patients.

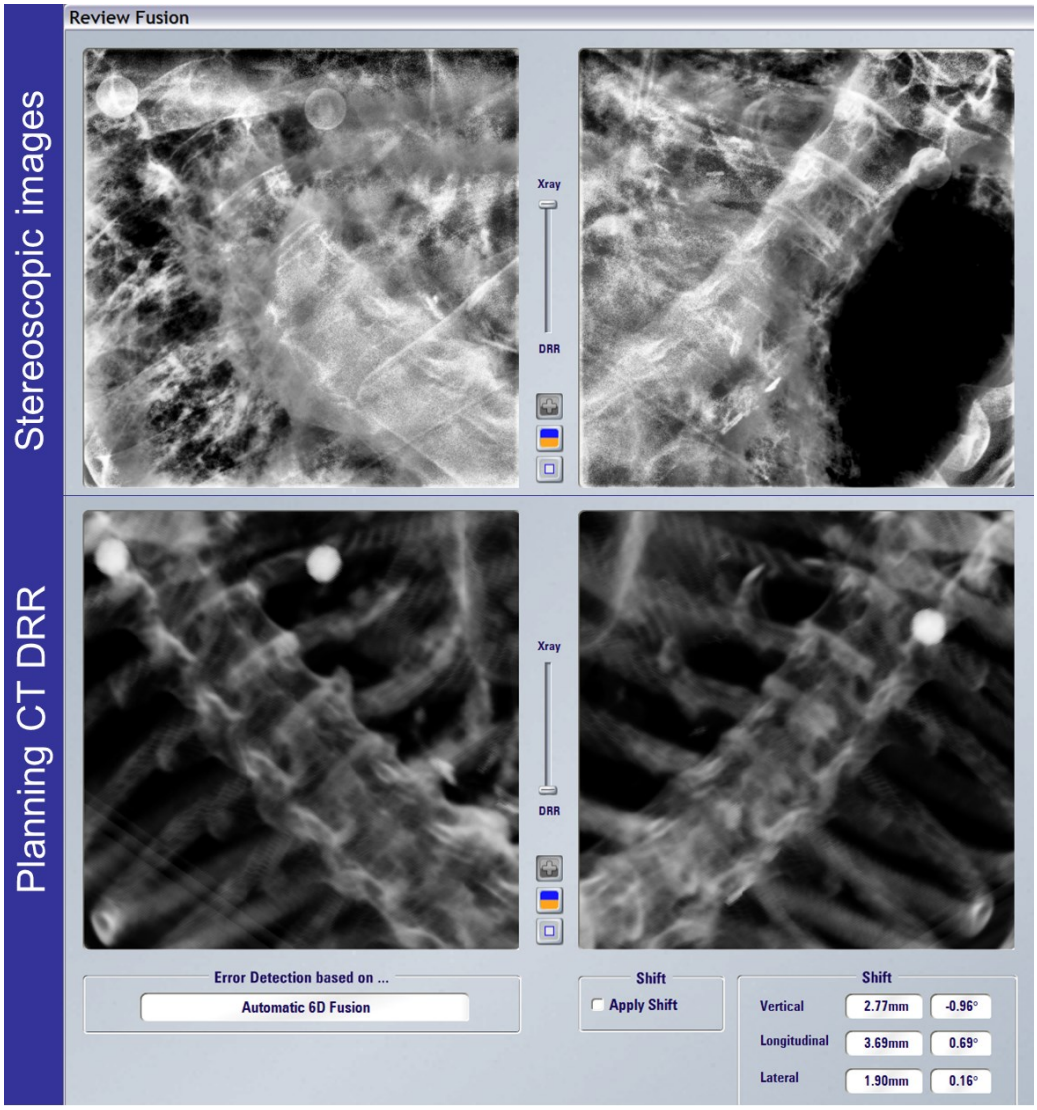

Figure 18 Matching spine with the stereoscopic imaging to treat a lung SBRT patient.

A total of 47 lung SBRT patients (214 treatment) were analyzed. The stereoscopic 6D spine matching data (Figure 18) was compared to that of CBCT soft tissue matching data. The CBCT matching data was assumed to be the ground truth and thus the ExacTrac alignment residual errors were calculated for all 6D. For every patient, the tumor distance from the spine was calculated, i.e. the distance between treatment and virtual isocenters.

Figure 19 illustrates the distributions of the residual errors for each 6D with the corresponding Gaussian fits. Ideally, this distribution should be a single spike at zero, i.e. stereoscopic spine alignment is identical to CBCT soft tissue matching. However, the actual distributions of the residual errors were centered around zero, but the non-zero standard deviations of the distributions suggested that some patients needed CBCT re-alignment. For each distribution, root mean square (RMS) error was also calculated. A larger Gaussian distribution standard deviation also indicates a larger RMS value.

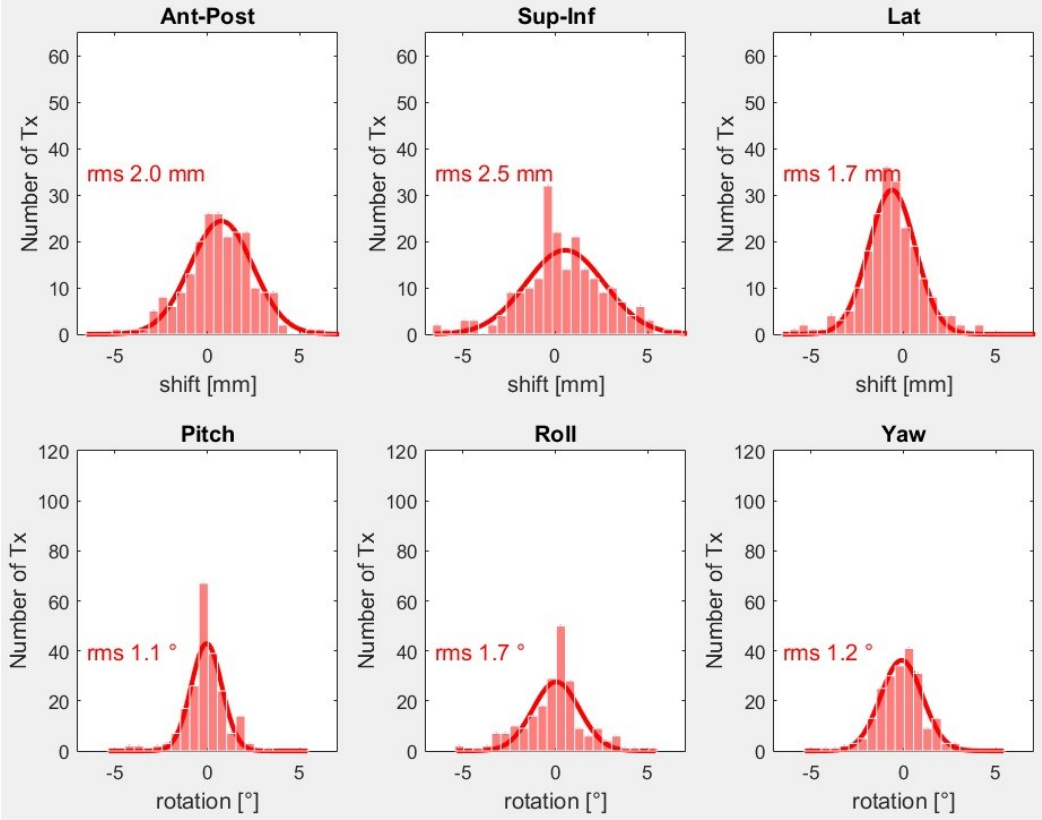

Figure 19 Residual errors in the 6D measured by CBCT soft-tissue matching following the ETX stereoscopic spine alignment. The solid red lines are Gaussian fist to each distribution. Root mean square (RMS) error is also reported for each plot.

In order to determine the number of treatments that needed CBCT re-alignment, the clinical thresholds (3 mm shift and 3° rotation) were applied to the distribution data. Based on these thresholds, 93 out of 214 treatments (43%) needed re-alignment. The number of treatments that needed to be re-aligned for each of the directions of motion is illustrated in Figure 20.

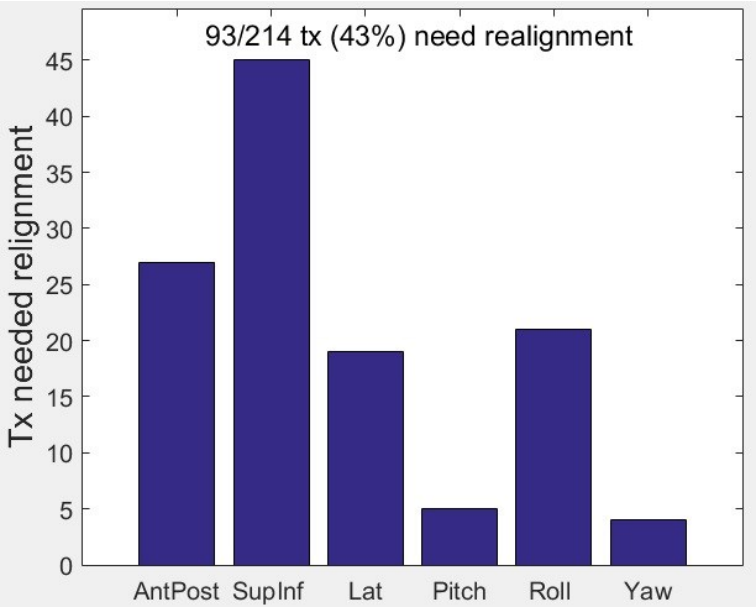

Figure 20 Treatments that required CBCT soft tissue re-alignment following stereoscopic spine alignment since spine alignment alone resulted in a larger than 3 mm error.

Most of the misalignment was in the superior-inferior (sup-inf), anterior-posterior (ant-post), and the roll directions, which had higher standard deviations of the residual errors. This is expected since a lung tumor is most likely to move in the sup-inf and ant-post directions due to respiratory motion.

Correlation between average individual residual errors and tumor distance from the spine for each patient is calculated and scatter plots are illustrated in Figure 21. One might hypothesize that the residual errors are smaller for those tumors that are closer to the

spine and thus stereoscopic imaging can replace CBCT for those cases. However, no correlation was found between the tumor distance from the spine and individual residual errors. This means that large residual errors can occur even for tumors closer to the spine.

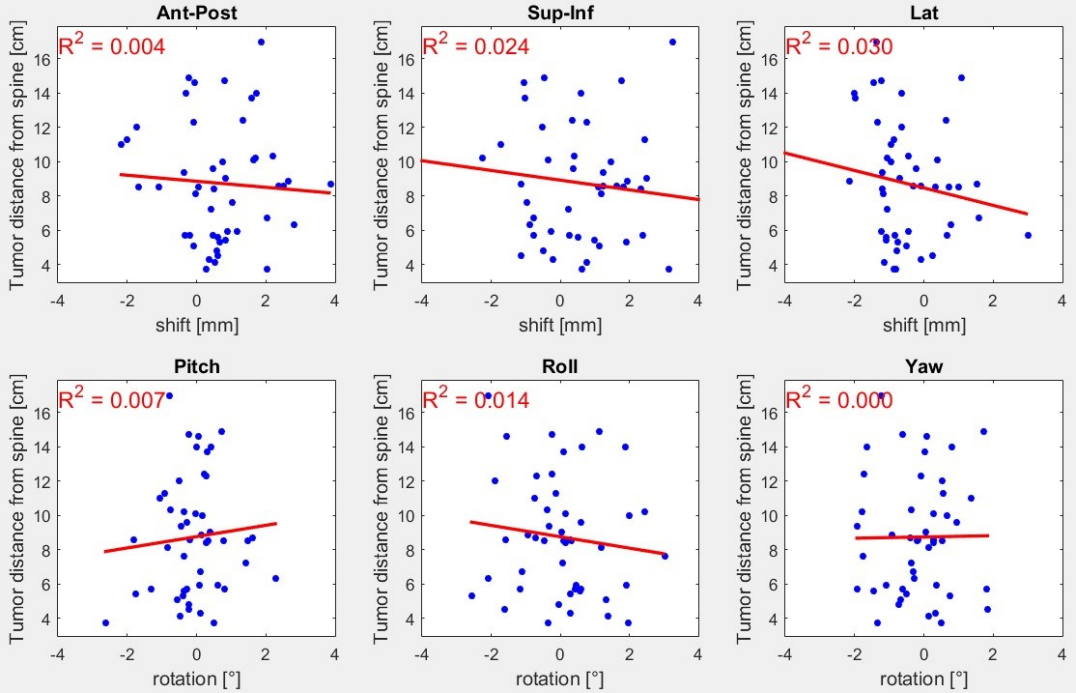

Figure 21 A scatter plot showing the lack of correlation between tumor distance from the spine and the residual errors.

Motivation for Dual-energy Stereoscopic Image Guidance

While ExacTrac stereoscopic imaging can offer quick pre-treatment patient alignment with minimal imaging dose, the above data demonstrates that bone matching based on spine imaging is not reliable for aligning lung SBRT patients. These patients require CBCT soft-tissue image registration as spine is a poor surrogate for lung SBRT patients' alignment, even for proximal tumors.

This motivates dual-energy imaging for the ExacTrac stereoscopic system, since DE imaging could allow for soft-tissue matching in these lung SBRT patients. Using DE imaging for soft-tissue weighted images, the lung tumors themselves could be matched to the corresponding soft-tissue DRRs instead of relying on the spine surrogate. There would be no need for the virtual isocenter, and the patient could be aligned to the treatment isocenter. This is more ideal, since the system would be aligning to tumor, which is what is to be treated. This would also eliminate the need for CBCT thus eliminating CBCT imaging dose.

CHAPTER 3: DEVELOPING DUAL-ENERGY STEREOSCOPIC X-RAY SYSTEM FOR THE EXACTRAC CLINICAL PLATFORM TO ENHANCE SOFT-TISSUE IMAGING

The content of this chapter is based on the following manuscript submitted to the journal of Medical Physics: "Optimizing dual-energy x-ray parameters for the ExacTrac clinical stereoscopic imaging system to enhance soft-tissue imaging", Wesley A. Bowman, James L. Robar, Mike Sattarivand

Introduction

Image guided radiotherapy (IGRT) is a clinical practice to ensure correct patient alignment for accurate dose placement on target while avoiding normal tissues. This is especially important in Stereotactic Body Radiation Therapy (SBRT), where a precise delivery of highly conformal hypofractionated radiation dose to target is needed to limit treatment volumes and normal tissue toxicity [14]. Image guidance could be achieved using an in-room stereoscopic x-ray imaging technique such as ExacTrac system (Brainlab AG, Germany). However, in conventional stereoscopic imaging, ribs and other bony anatomy may overlap with soft-tissue and tumor which may cause difficulty and inaccuracies in target alignment. Dual-energy imaging may be a solution to address this issue and allow better accuracy in patient alignment.

Dual-energy (DE) imaging can create soft-tissue-weighted or bone-weighted images by utilizing the differences in atomic number of bone and soft tissue and the energy dependence of their attenuation coefficients [1]. The simplest way to produce a soft-tissue DE image is with simple log subtraction,

$$\log(I_{DE}) = \log(I_{HE}) - w\log(I_{LE})$$

where I_{DE} is the DE image, I_{HE} and I_{LE} are the HE and LE images, and w is the relative weighting factor. With optimal choices of imaging parameters, soft-tissue-weighted (or bone-weighted) DE images can be created. The parameters of interest are tube potential and mAs (for low and high-energy) as well as weighting factors. The use of a filter for the DE imaging could increase spectra separation and improve the image quality, thus filter material (based on Z) and thickness could also be optimized.

Various previous studies have been reported on DE imaging in radiography and optimizing parameters for different systems. Shkumat *et al* explored optimizing DE parameters to maximize the detection of lung nodules in DE chest radiography using a Kodak RVG-5100 digital imaging system [15]. Richards *et al* optimized DE imaging with a Varian x-ray tube and an indirect flat panel detector used for chest radiography [16]. Primak *et al* examined additional filtration for DE dual-source computed tomography (CT) [17]. They reported that tin was an ideal filter material to increase DE contrast when added to the high-energy x-ray tube.

Studies on DE imaging for IGRT applications are scarce. Perhaps the first application of DE for IGRT was reported by Hoggarth *et al* who optimized DE imaging parameters for

the On-Board Imager (OBI, Varian Medical Systems, Palo Alto, CA) without filters [18]. Using these parameters for OBI, Sherertz *et al* demonstrated the clinical feasibility of DE imaging to enhance lung tumor localization in 10 patients [19]. Patel *et al* also reported on the efficacy of DE fluoroscopy using the OBI for markerless motion tracking of lung tumors [20]. A similar study used 1 mm of additional tin filtration for the high-energy (HE) beam and no filtration for low-energy (LE) on the Elekta x-ray volume imaging (XVI) system (Elekta AB, Stockholm, Sweden) [21]. The use of tin filtration on the HE beam allowed for an increase in spectral separation between the high and low-energy spectra. Optimized parameters for DE imaging are often geometry and system dependent. To the best of our knowledge, no previous DE optimization study has been reported for the ExacTrac stereoscopic imaging system.

For applications such as lung SBRT, where real-time imaging is beneficial, fast image acquisition is desirable due to respiratory motion. A single filter for both high and low-energy would more easily allow for fast-kVp switching, since mechanically switching filters is often slower than electronically switching tube potentials. Fast kilovoltage switching allows for both the high and low-energy images to be acquired nearly simultaneously with one tube and a detector [22]. The objective of this work is to optimize DE imaging parameters for ExacTrac stereoscopic imaging system and identify an optimal single material and material thickness to filter the beams.

Materials and Methods

Simulation Study

Spektr simulations [23] were used to identify a filter material in the atomic number (Z) range of 3 to 83 based on a metric defined to separate spectra of high and low energies. Spektr is based on a tungsten anode spectral model using interpolating polynomials (TASMIP) [24] and has been reported to be in excellent agreement with the measured spectra for tube potentials between 30-140 kVp [25]. Spektr parameters were tuned and validated using half-value layer (HVL) measurements of the ExacTrac tube. The HVL values were measured using a calibrated RaySafe detector (Unfors RaySafe AB, Billdal, Sweden) in a narrow beam geometry by adding additional collimators. The inherent filtration of Spektr generated spectra varied such that the HVL values of the spectra matched the measured HVLs for all tube potentials in the range of 60 to 140 kVp. The generated spectra were used to optimize the filter material.

To quantify the HE and LE spectra separation, a metric was defined based on spectrum-weighted linear attenuation coefficients for bone:

$$\bar{\mu}(E) = \frac{\int \Phi(E) \cdot \mu(E)\, dE}{\int \Phi(E)\, dE}$$

where $\Phi(E)$ is the fluence spectrum and $\mu(E)$ is the linear attenuation coefficient for bone. The overall metric, called the Energy Ratio (ER), is then calculated by the ratio of low to high energies:

$$ER = \frac{E(\bar{\mu}_{LE})}{E(\bar{\mu}_{HE})}$$

where $E(\bar{\mu}_{HE})$ and $E(\bar{\mu}_{LE})$ are the energies evaluated at the particular values (HE and LE) of the spectrum-weighted linear attenuation coefficient ($\bar{\mu}(E)$).

This metric not only includes spectrum variation with energy, but also non-linear variation of bone μ with energy. The values used for μ were based on data from National Institute of Standards and Technology (www.nist.gov) implemented in Spektr. The highest value of the ER is unity when the same tube potential is used for both HE and LE. As the ER decreases below unity, the separation between the two spectra increases. The ER was used to identify the optimal filter material for generating soft-tissue-weighted DE images.

Lung Phantom Study

A lung phantom (Figure 22) was constructed and used to optimize filter thickness, tube potentials, and weighting factors to obtain bone subtracted DE images. The phantom was based on previous work by Shkumat *et. al* [15] and the American Association of Physicists in Medicine (AAPM) report 31 [26]. The phantom design was modified to match limited field of view (FOV) (~13 cm) and the oblique geometry of the ExacTrac system. The phantom consisted of different layers for bone, tumor, and soft tissue. The bone layer had two 2 cm thick bone equivalent material inserted in a 2 cm layer of Solid Water™ (Gammex, Middleton, WI). Behind the bone layer was a layer of tumors made of Solid Water in varying sizes. Each tumor was a cylinder with a height equal to its diameter. The diameter of the tumors ranged from 1 to 2 cm. The tumors were attached to the posterior side of the bone layer. The remaining was three layers of 5 cm thick Solid Water (total 15 cm). The ExacTrac beam approaches isocenter from a 45° angle with

respect to the vertical plane along the couch (when couch is at 0°) and at a 42° angle from the floor (see Figure 22). Therefore, to take the phantom images, the couch was rotated to 45° and the stand made a 42° angle with the table to ensure the incident beam was perpendicular to phantom surface.

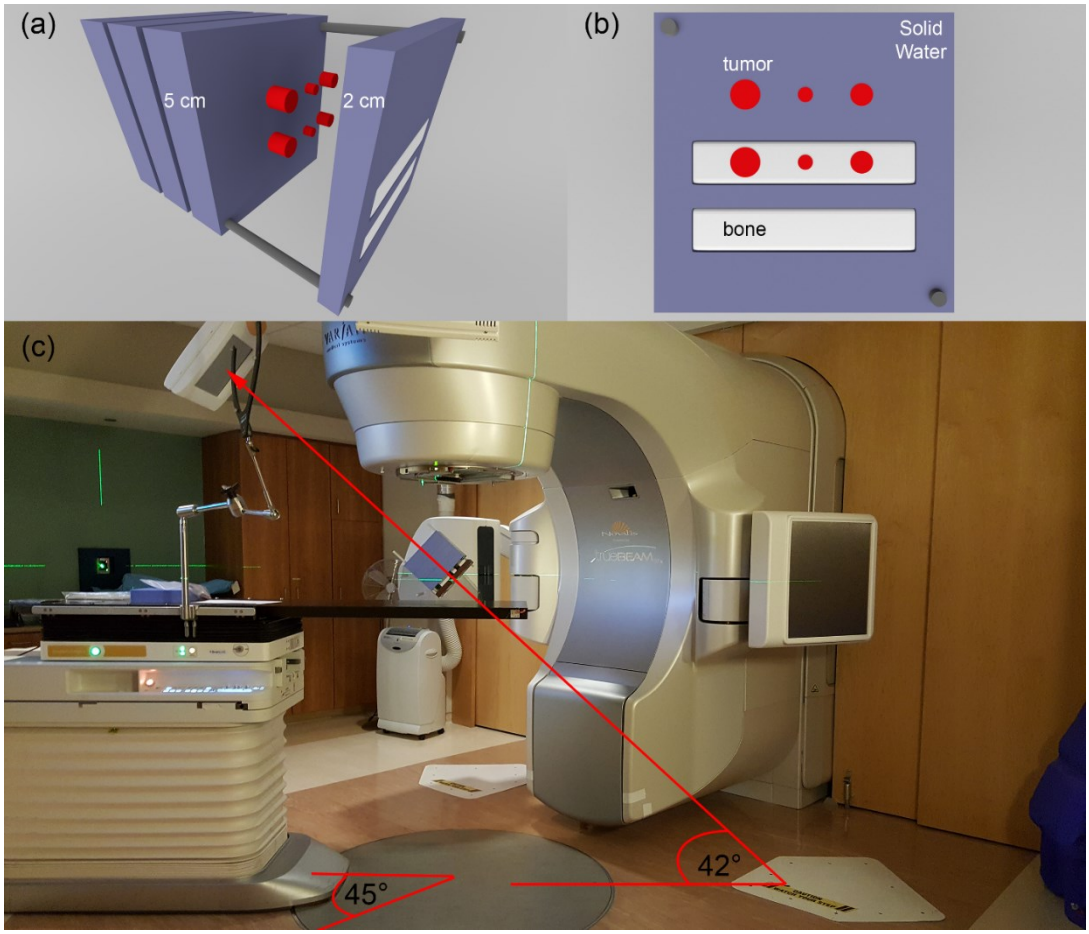

Figure 22 A 3D model of the lung phantom that was constructed for the experiments (a). The blue material is Solid Water slabs, the red material is the tumor model (made of Solid Water), the white material is bone equivalent material, and the grey material is rods that hold the phantom together. The 3D model illustrates (a) a perspective view of the lung phantom, (b) the front view of the lung phantom, and (c) the actual phantom on the treatment couch.

The lung phantom was imaged with tin filter thicknesses ranging from 0 to 1 mm using various kVp ranges of 60 to 80 for LE and 120 to 140 for HE. Tin filter thickness were the same for both LE and HE. Images were exported from the ExacTrac workstation into in-house software developed in Matlab (MathWorks, Natick, MA, USA) to calculate DE image. To reduce noise amplification during DE subtraction, an anti-correlated noise reduction (ACNR) algorithm [5] [6] [7] was implemented using parameters from Richard *et al* [8]. For soft tissue DE imaging, ACNR significantly suppresses noise with minimal reduction in modulation transfer function (MTF) [8]. The weighting factor for DE subtraction varied in the range of 0 to 1. A cost function was defined to quantify the best DE parameters. The cost function was calculated by:

$$Cost = CNR_{b_{st},st} + \frac{1}{CNR_{b_t,b_{st}}} + \alpha\left(\frac{\sigma_{st}}{\overline{I_{st}}}\right)$$

where $CNR_{b_{st},st}$ is the contrast-to-noise-ratio (CNR) of the soft-tissue overlapped by bone to soft-tissue without overlap (Figure 30), $CNR_{b_t,b_{st}}$ is the CNR of the tumor overlapped by bone to bone overlapped by soft-tissue, α is an empirical factor to amplify the noise term, σ_{st} is the standard deviation of the soft-tissue region-of-interest (ROI), and $\overline{I_{st}}$ is the mean intensity of the soft-tissue ROI. The empirical factor is needed for the noise term in order to amplify the noise contribution to the cost function. This ensures that a high penalty is placed on having a large amount of noise in the image. For the ACNR implementation in DE algorithm, α was determined to be 30. The definition of CNR used was:

$$CNR_{a,b} = \left| \frac{I_a - I_b}{\sqrt{\frac{1}{2}(\sigma_a^2 + \sigma_b^2)}} \right|$$

where I_a and I_b is the average intensity of two ROIs with the corresponding standard deviations σ_a and σ_b, respectively. The three terms in the cost function are defined to minimize the bone contrast in DE image (1st term), maximize the tumor visibility behind the bone (2nd term), and minimize the overall noise content (3rd term). The cost function was used to identify the optimal weighting factor, filter thickness and kVp pair.

Anthropomorphic Phantom Study

Using the optimized parameters from the lung phantom, DE images of an anthropomorphic Rando phantom [27] with a soft-tissue-equivalent spherical tumor inserted in the lung (Figure 23) were acquired. DE images were calculated as per the lung phantom. For the Rando phantom, the weighting factors were qualitatively determined by trial and error such that the DE image had best bone cancelation with minimum quantum noise.

Figure 23 The Rando phantom and the spherical tumor inserted in his lung.

Dose Measurements

Using a calibrated RaySafe detector, dose was measured for clinical single energy (SE) chest imaging protocol (kVp=120, mAs=20), for the DE technique using 0.3 mm tin filtering, and for the DE technique with no filtering. The tube mAs values were adjusted for both the high and low energy beams such that DE imaging dose with no filtration was matched with the 0.3 mm tin filter DE imaging dose. The dose of the non-filtered DE image was lowered to match the filtered DE image since the filtered DE image could not be brought up in dose due to the mAs constraints of the ExacTrac system. The parameters for the unfiltered images were 140 kVp at 1.59 mAs for the high energy and 80 kVp at 19.80 mAs for the low energy. These kVp values were obtained from the experimental results of the cost function. The parameters for the 0.3 mm tin filtered

images were 140 kVp at 19.80 mAs for the high-energy and 80 kVp at 41.58 mAs (maximum allowed mAs) for the low energy. The dose was calculated using

$$D_{w,z=0} = A \cdot B_w \left[\left(\frac{\bar{\mu}_{en}}{\rho}\right)^{w}_{air}\right]$$

where $D_{w,z=0}$ is the surface dose to water at detector location (isocenter), A is the air kerma measured with the RaySafe detector, B_w is the backscatter factor, and $\left[\left(\frac{\bar{\mu}_{en}}{\rho}\right)^{w}_{air}\right]$ is the ratio of the average mass energy-absorption coefficients of water to air. The dose calculation formalism above is based on AAPM Task Group (TG) 61 [28] while the stem effect was ignored for simplicity. The values used in the equation for 80, 140, and 120 kVp are listed in Table 1. The ExacTrac 13x13 cm^2 square field at isocenter was converted to equivalent circular field (14.67 cm diameter) using "the same area" principle.

Table 1 A list of parameters used in the dose calculation for different tube potentials using 220 cm SSD and a field equivalent diameter of 14.67 cm.

kVp	HVL	B_w	$(\mu_{en}/\rho)^{w}_{air}$
80	4.230	1.442	1.027
140	6.753	1.506	1.040
120	6.000	1.487	1.034

The backscatter factors were linearly extrapolated from the highest source to surface distance (SSD) in TG61 (100 cm) to ExacTrac SSD (~220 cm). The B_w values in TG61 varied by only ~2% when the SSD changed from 50 to 100 cm.

Results

Simulation Study

Figure 24 is a plot of measured HVL as a function of tube kVp in comparison to Spektr calculated HVLs. The plot illustrates that the measured HVL values are in good agreement with those generated by Spektr simulation. To achieve this agreement, the simulated spectra were generated using 3.9 mm Al of inherent tube filtration.

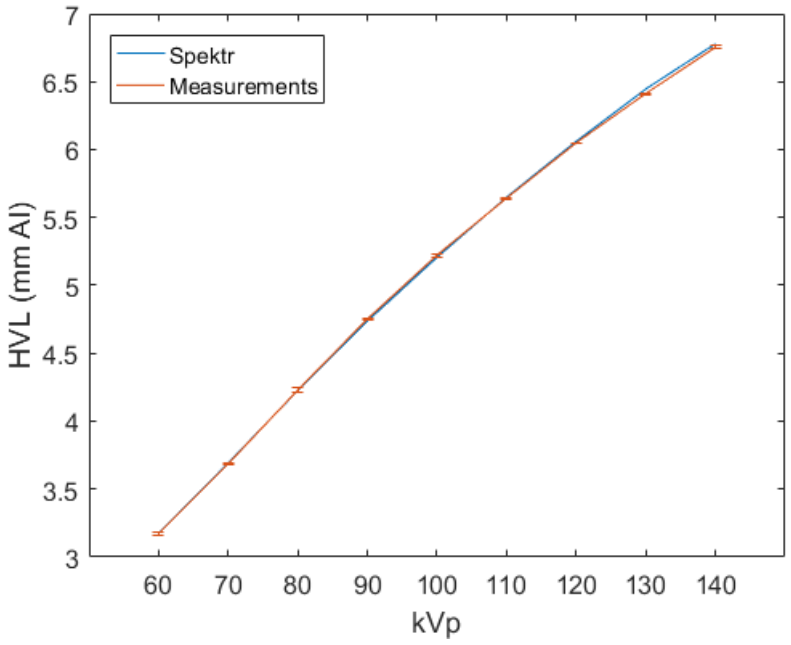

Figure 24 Spektr generated HVL values compared with measured narrow-beam geometry ExacTrac HVLs. Standard deviations (error bars) were calculated from multiple HVL measurements.

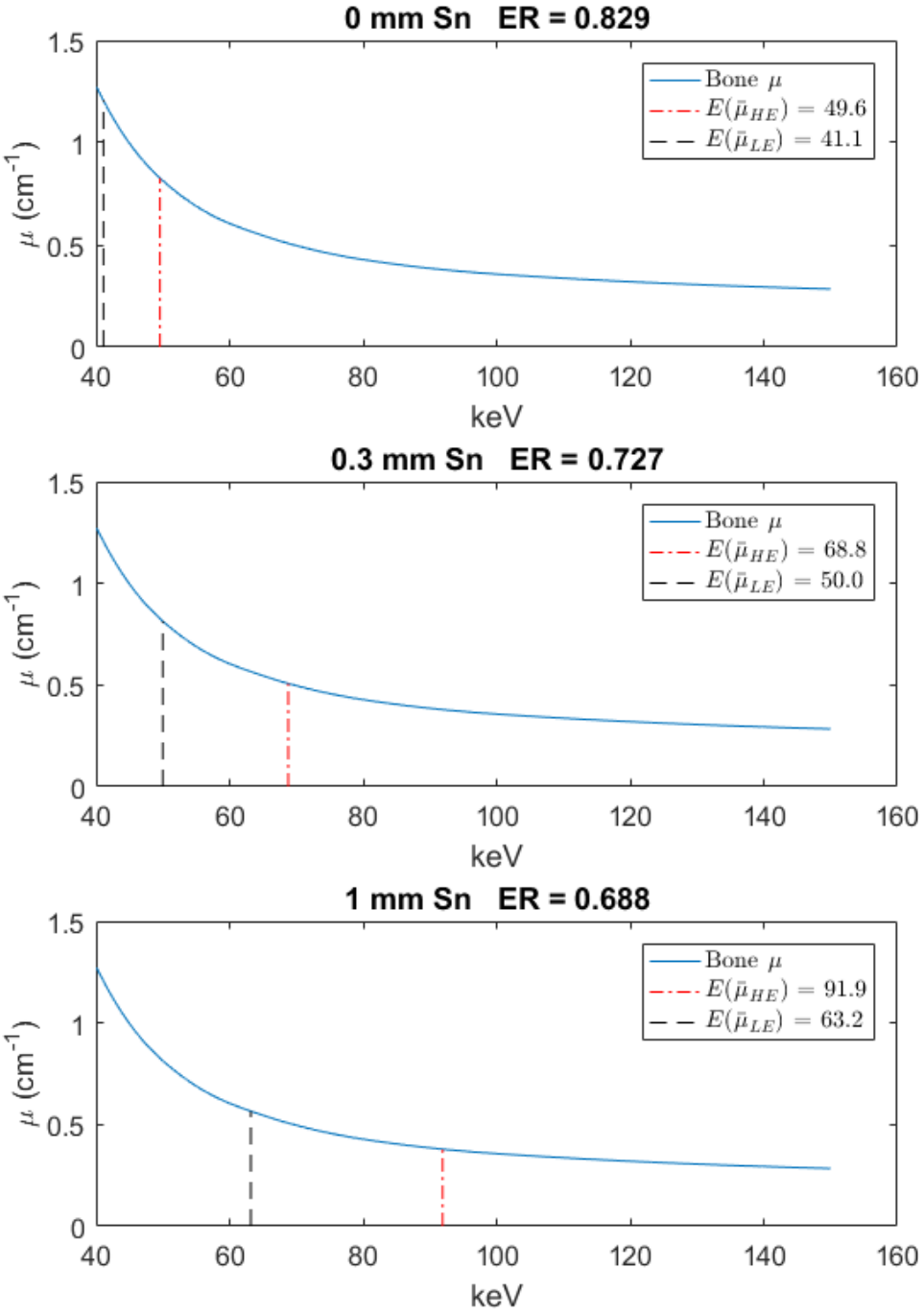

Figure 25 Plots of bone linear attenuation coefficients with the ER components with and without tin filtration for HE=140 kVp, LE=80 kVp, indicating separation of the high and low effective energy as more filtration is added.

Figure 25 illustrates the plots of linear attenuation coefficients for bone with $E(\bar{\mu}_{HE})$ and $E(\bar{\mu}_{LE})$ marks on the curves for three different thicknesses of tin (0, 0.3, and 1 mm). The further separated the two components of the ER are, the more separated the spectra will be. Figure 26 illustrates Spektr simulated spectra of HE and LE for the corresponding tin filters. The spectra are visually more separated as more tin is added, which is confirmed by the ER in Figure 25.

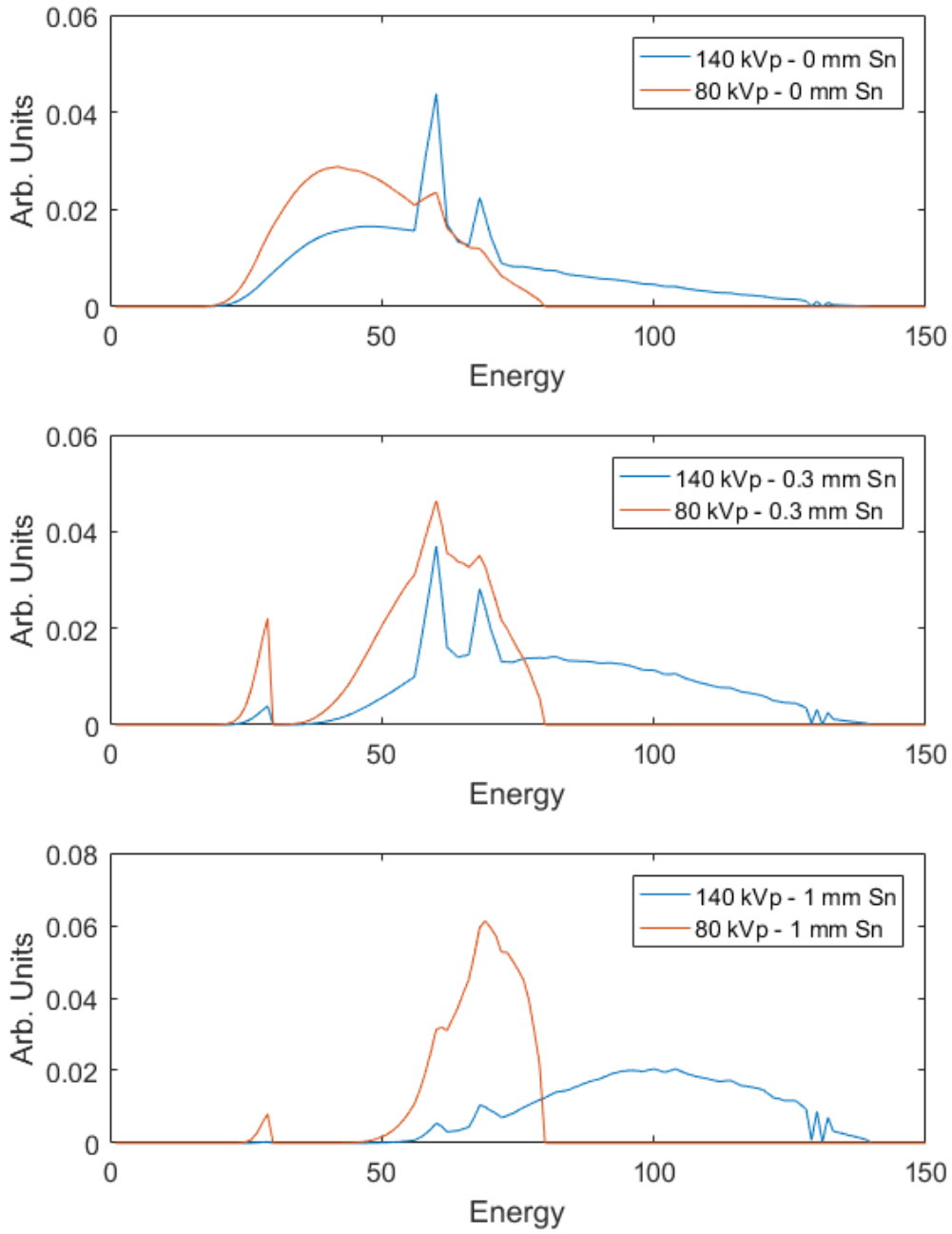

Figure 26 Simulated spectra with and without tin filtration illustrating that there is a separation of the spectra as more filtration is added to both HE and LE. Each spectrum is normalized to unit area.

Figure 27 illustrates the trend of the ER as a function of filter atomic number. Materials that were liquid or gas at room temperature were not included in Figure 27, because they are not practical to use as a filter. For this reason, there are gaps in the trend in Figure 27. The ER determined that praseodymium (Z = 59) was the material that provided the best energy separation. However, praseodymium is a lanthanide, highly reactive, and considered mildly toxic. All of the materials from Z=51 to 69, that had a smaller ER than tin, did not appear suitable clinical candidates because of their limited availability and chemical properties being similar to praseodymium, i.e. highly reactive and/or toxic. Tin (Z = 50) was chosen as the material of choice for filter that provided the best energy separation (ER), non-toxicity, non-reactiveness, and accessibility. The overall trend of the ER vs atomic number was the same, regardless of the filter thickness. The ER is an idealized approximation of the spectra separation, and thus only the material choice was identified using the ER, and not the filter thickness, kVp, or mAs of the beams.

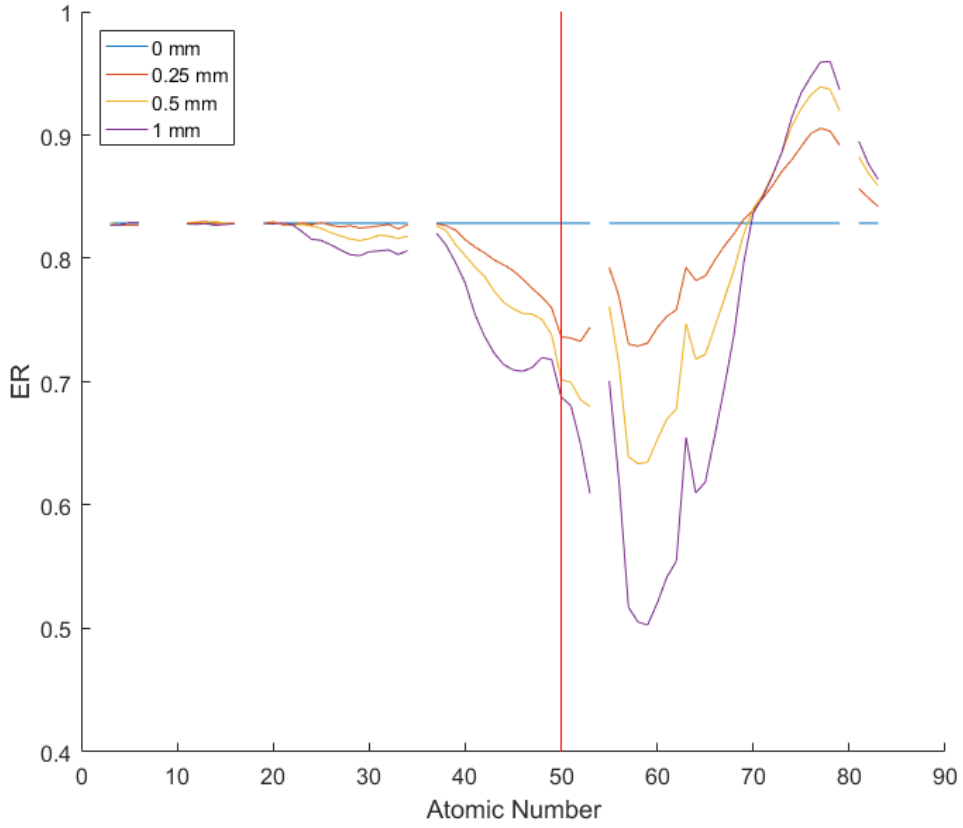

Figure 27 The ER as a function of filter atomic number illustrating that the overall trend does not change with the thickness of the filter. The red vertical line represents tin.

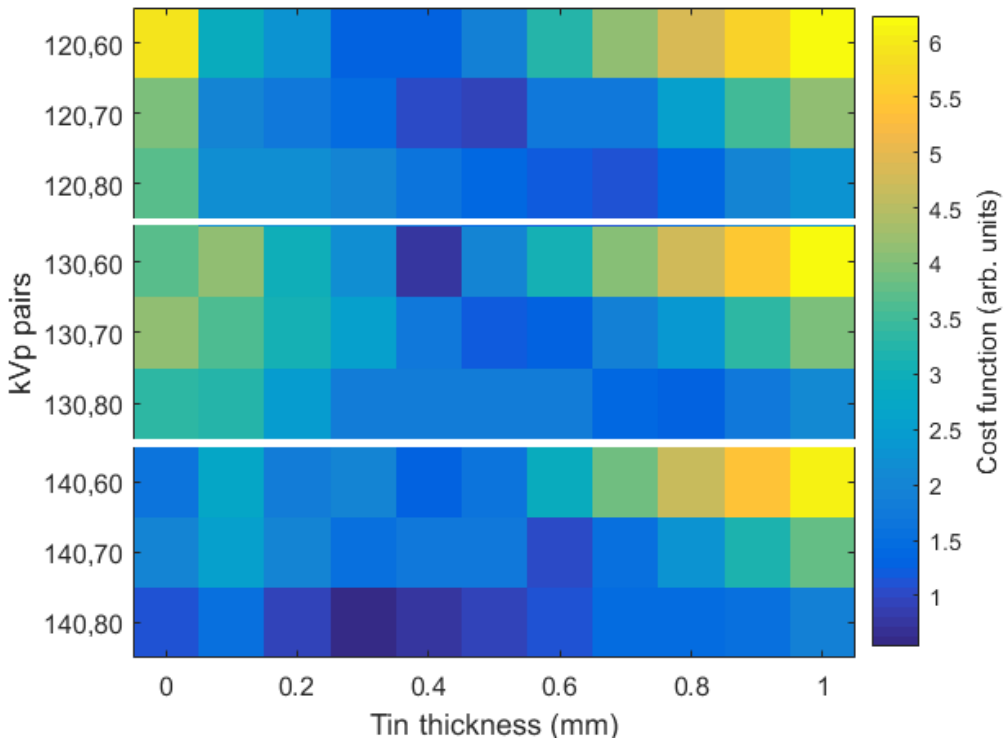

Figure 28 Values of the cost function for different DE kVp pairs vs tin thicknesses illustrating that (140, 80) kVp pair at 0.3 mm of tin scored the lowest.

Lung Phantom Study

Figure 28 illustrates the values of the cost function as a function of tin thickness and DE kVp pairs. Based on these values, lower kVp values for LE (e.g. 60) should be avoided as they do not yield enough signal in the detector. The cost function identified the best soft-tissue-weighted image in the lung phantom was achieved using 0.3 mm tin and a tube potential pair of 140 for HE and 80 for LE. Figure 29 illustrates the components of the cost function at three different tin thicknesses for a tube potential pair of 140 and 80. At lower tin thicknesses, bone contrast (the first term in the cost function) is the dominant factor. However, at higher tin thicknesses, tumor contrast and noise (2^{nd} and 3^{rd} terms) also play an important role to achieve minimal cost function. Figure 30 compares images

acquired with a single energy to those acquired with DE, with and without tin filter. Both DE techniques achieved soft-tissue-weighted images. However, in comparison to DE with no filtration, the DE image with the filtration showed noticeable improvements on bone cancelation, tumor contrast, and noise content.

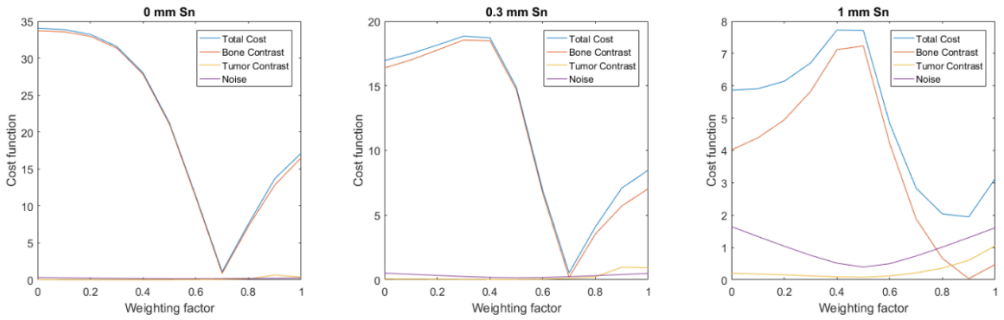

Figure 29 The components of the cost function are illustrated at three different thicknesses of tin for HE=140 kVp, LE=80 kVp.

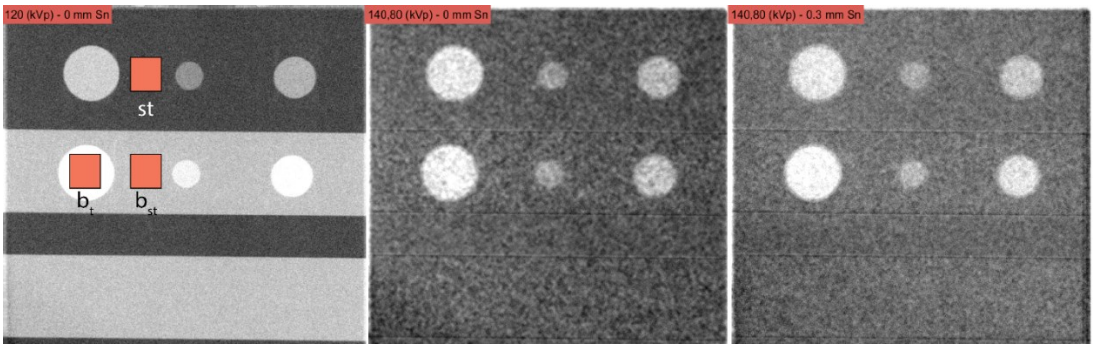

Figure 30 A comparison of the lung phantom imaged with SE (left) and DE techniques with zero (middle) and 0.3 mm (right) of tin filter. The clinical SE image illustrates the location of the bone strips, tumor, and ROIs. The imaging dose for both the filtered and unfiltered images was the same.

Anthropomorphic Phantom Study

DE images of the Rando phantom with and without tin filtering are illustrated in Figure 35 in comparison to the clinical 120 kVp single energy image. DE images with tin filtration showed noticeable bone elimination and improvements in noise and tumor contrast when compared to images acquired without filtration.

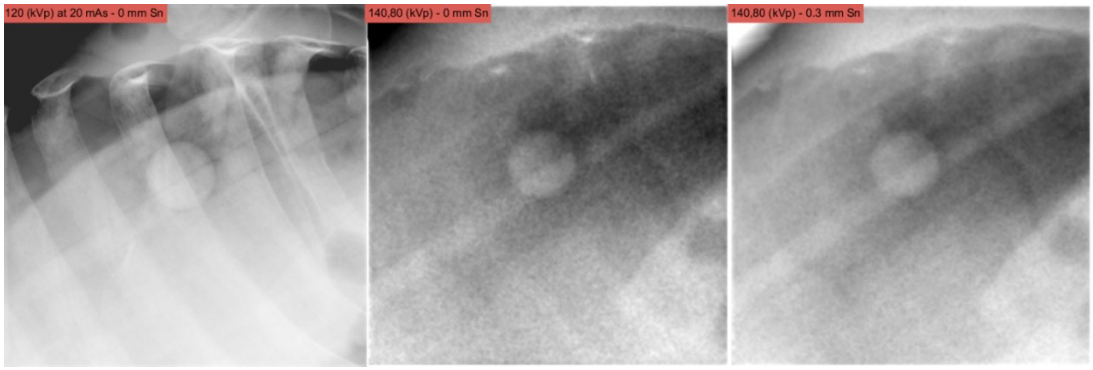

Figure 31 A comparison of the Rando phantom with the single energy clinical image (left) and the DE image without (middle) and with tin filtering (right). The spherical lung tumor model is also indicated behind the rib bone. With tin filtering, there are noticeable improvements in bone subtraction, tumor contrast, and noise content. The imaging dose for both the filtered and unfiltered images was the same and approximately 80% of clinical single energy imaging dose.

Dose Measurement Results

The measured surface dose for the ExacTrac clinical single energy (SE) chest imaging protocol was approximately 445 μGy per stereoscopic view. Using 0.3 mm of tin, the DE

dose reduced to approximately 354 μGy. The DE dose with no filtration was then lowered (by adjusting the mAs) to be the same as the 0.3 mm thickness.

Discussion

In this study, the feasibility of DE imaging on the ExacTrac stereoscopic imaging system was demonstrated. The technique can be incorporated into the existing clinical stereoscopic imaging system requiring mainly a software update. Dual-energy imaging could be used in daily IGRT to enhance tumor and soft-tissue visibility, whereas SE imaging is often limited to using a bone surrogate for tumor alignment. Stereoscopic system provides two virtually simultaneous views to infer 3D image guidance information; a feature that is lacking in OBI based orthogonal kV planar imaging. Although OBI can obtain 3D volumetric images through cone-beam CT (CBCT), using a stereoscopic system has its own inherent advantages over (CBCT) for image guidance. Image acquisition is much faster in the stereoscopic system taking less than a second, while CBCT requires about 40-60s to acquire a full 3D imaging set and necessitates treatment interruption. Image processing time for tumor alignment is also much faster for projection 2D images than for CBCT 3D volumetric images. Moreover, unlike the OBI based kV imaging where only a single projection image is available, the stereoscopic imaging obtains 3D information from two 2D projection images. This feature could be explored for tumor tracking during treatment without treatment interruption. This concept has been recently applied for prostate motion tracking using fiducial markers on ExacTrac system [29]. With the addition of DE using fast-kVp switching, real-time

markerless-motion tracking of the tumor may be achieved with stereoscopic imaging during treatment.

Fast kilovoltage switching is already employed in commercial DE CT scanners, with the ability to switch between 80 and 140 kVp in less than 0.5 ms [22]. Fast-kVp switching is desired in stereoscopic lung imaging to obtain near real-time high and low-energy images for both stereoscopic views to minimize tumor respiratory motion. A single filter for both HE and LE tube potentials is advantageous and robust as it avoids a mechanical switch to swap the filters which must be coordinated with the fast-kVp switching system. DE imaging is possible without adding any beam filtration, however, using filtration adds further separation of the spectra and leads to improvements in the DE images, such as better bone elimination or reduced noise in the image.

The HVL measurements were performed to gain confidence that Spektr simulation was providing accurate energy spectra for various kVp settings (Figure 24). The spectra were used to calculate the ER, while images from the lung phantom were used to calculate the cost function. The main difference between the two is that the ER did not take into account the mAs and scatter since Spektr simulates the primary beam only. This meant that the ER was an ideal approximation of the separation of the spectra of the primary beam, and could not be solely used without experimental proof. The ER was also calculated for all the kVp pair choices in the range 60 to 140 (data not shown). The trend of the ER always showed that the kVp pair with the highest separation produced the most separated spectra as expected, i.e. 140 for HE and 60 kVp for LE in our case. Therefore, to optimize kVp and filter thickness, the lung phantom data were used.

Dual-energy requires two x-ray exposures at the high and low-energies. This could be expected to increase the dose to the patient, especially in a stereoscopic setup since two views are needed to obtain the 3D information. However, in this study, the tube potential and mAs have been optimized, and the DE imaging dose is still less than that of the clinical single energy image. The addition of the tin filtration also lowers the dose since it attenuates some of the low energy beam. Despite limiting the parameters to assure the clinical dose is not exceeded, it was still possible to obtain a DE image with enhanced soft-tissue contrast. Imaging dose from the stereoscopic DE imaging is comparable to orthogonal kV planar imaging (1 - 3 mGy) while it is less than that of CBCT (16 - 23 mGy) [30]. However, lower imaging dose is always desirable and should be kept in mind when developing new techniques.

Due to mAs limitation on ExacTrac system, the DE imaging dose could not be increased to match the clinical SE imaging dose. Even though both HE and LE beams are being attenuated by the tin filter, the LE image was always acquired at maximum tube mAs, which meant that the fluence could not be compensated for the addition of more filtration. The HE was limited by the detector saturation while the LE was limited by the mAs settings on ExacTrac tubes. An increase in mAs would allow for the imaging dose to approach the clinical single energy dose, which would increase the quality of all the DE images.

The optimized imaging parameters (tube potential and mAs) described in this work were higher than previous studies for DE chest imaging, which are listed in Table 2. This is partially due to the fact that the same filtration was used for both high and low energies,

which meant the low-energy had to be adjusted to a higher kVp to penetrate the filter material and a higher mAs to obtain more fluence on the detector. The oblique geometry in ExacTrac imaging would also contribute to an increase in parameters. In this geometry, the beam is not going through simple anterior-posterior (or lateral) directions, but rather the oblique entry through the patient increases the beam path length.

Table 2 A list of the dual-energy parameters from the previous studies.

Author	HE	LE	Comment
This study	140 kVp at 19.8 mAs	80 kVp at 41.58 mAs	ExacTrac, 0.3 mm tin for both HE and LE
Patel *et al* [20]	120 kVp at 1.5 mA	60 kVp at 6 mA	OBI, Fluoroscopy – no filtration
Sherertz *et al* [19]	120 kVp at 1 mAs	60 kVp at 4 mA	OBI, Fluoroscopy – no filtration
Hoggarth *et al* [18]	140 kVp at 1 mAs	60 kVp at 3.2 mAs	OBI – no filtration
Menten *et al* [21]	140 kVp at 2.5 mAs	70 kVp at 1.5 mAs	XVI, 1 mm tin on HE
Williams *et al* [31]	130 kVp at [10-25] mAs	60 kVp at [1.6-5] mAs	Kodak RVG-5100 – no filtration
Richard *et al* [16]	150 kVp at [1-4] mAs	60 kVp at [2-5] mAs	Rad 94 - sapphire housing, no filtration
Shkumat *et al* [15]	130 kVp at [16,25,50] mAs	60 kVp at [3.2, 5, 10] mAs	Kodak RVG-5100 – no filtration

Conclusions

Dual-energy soft-tissue imaging is feasible using the ExacTrac stereoscopic imaging system, without increasing the clinical imaging dose, utilizing optimized acquisition parameters with no beam filtration. With the addition of a single tin filter for both high and low energies, noticeable improvements on bone elimination, tumor contrast, and noise content are realized with optimized parameters. The clinical implementation of DE

on stereoscopic imaging systems may improve lung tumor visibility and may provide a potential means for increased accuracy in patient alignment and tumor tracking.

CHAPTER 4: CONCLUSION

While much has been achieved to fulfill the objective of this thesis, there is still more undertaking needed to expand upon the aims of this work. Below a few proposals are presented for the future directions of this work, but first we discuss some potential limitations.

Potential Limitation to Dual-energy Imaging

A potential limitation to dual-energy imaging is an inherent limitation to all x-ray imaging, which is subject contrast. Subject contrast is the contrast that arises in the x-ray signal after it has interacted with the patient, but before it has been detected [1]. A simulation was done to see how the patient's thickness would affect the subject contrast, which is the ideal scenario for x-ray imaging. For this particular simulation, the subject CNR was used.

$$CNR_s = \frac{A - B}{\sqrt{\frac{1}{2}(\sigma_A^2 + \sigma_B^2)}}$$

where σ_A and σ_B are the standard deviations of A and B, respectively. An illustration of the setup for the simulation is shown in Figure 32. A tumor was placed in lung tissue, which was surrounded by soft-tissue. To increase the patient's thickness, the soft-tissue was varied from 5 to 30 cm. The lung tissue was 20 cm and the tumor was 2.5 cm. The

two arrows represent the path of attenuation that was simulated. The path through only lung and soft-tissue was defined as

$$I_L = I_0 e^{-\mu_L t_L - \mu_S t_S}$$

where μ_L and μ_S are the linear attenuation coefficients for lung and soft-tissue respectively, and t_L and t_S represent the thickness of tissue for lung and soft-tissue, respectively. The path through the lung tissue, tumor, and soft-tissue was defined as

$$I_T = I_0 e^{-\mu_L t_L - \mu_S t_S - \mu_T t_T}$$

where μ_T and t_T were the linear attenuation coefficient and thickness of the tissue of the tumor. Poisson statistics were assumed making the variance equal to the mean for each signal.

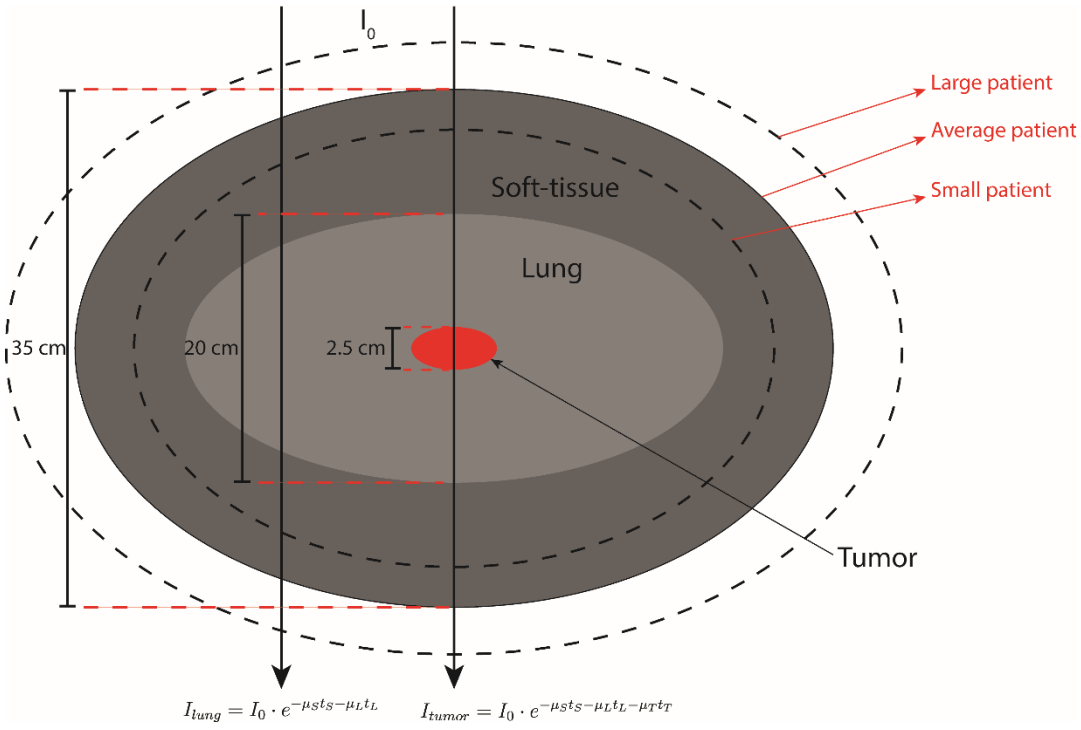

Figure 32 An illustration of the simulation done to calculate the subject contrast for a varying thickness patient. The soft-tissue portion was varied in thickness, which increases the total patient thickness.

Using these two intensities coming out of the patient, the subject CNR was calculated for the varying thickness of the patient, and the resulting plot is shown in Figure 33. Here, the subject CNR has been normalized to 35 cm, which is assumed to be the average patient thickness.

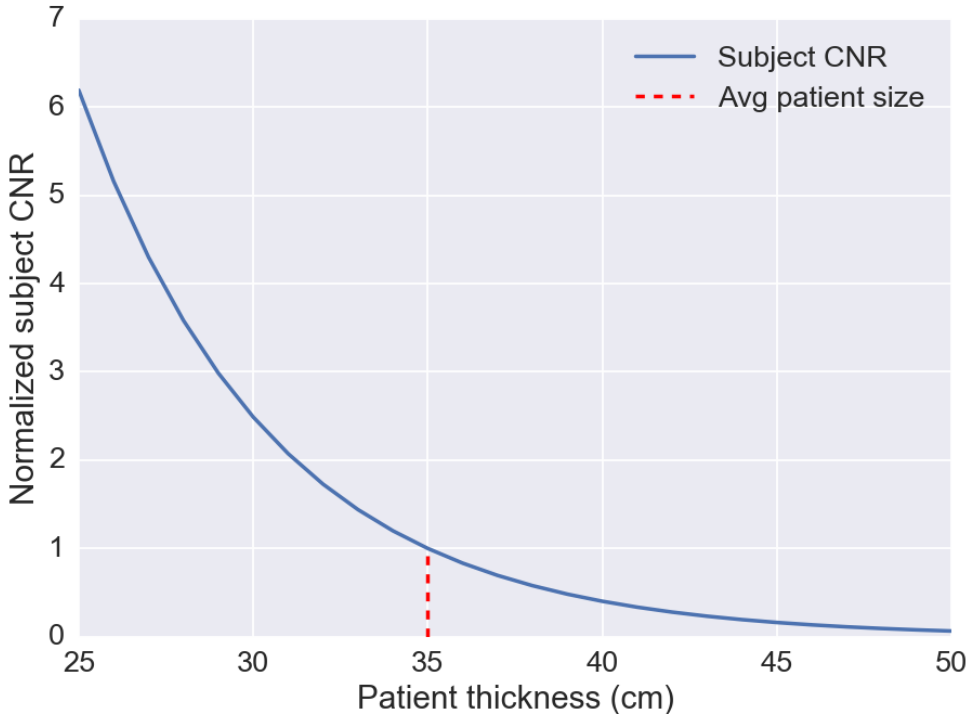

Figure 33 The subject CNR slowly decays to zero as the thickness of the patient increases.

As the thickness of the patient increases, the subject CNR decreases toward zero. This means that as we have thicker and thicker patients, there will not be enough contrast to get a good x-ray image. This will affect the DE images as well, reducing the overall signal to visualize the tumor. This is not a limitation of DE imaging per se, but rather is inherent for x-ray imaging in general and is due to overlapping soft-tissue. Application of DE imaging is expected to improve the CNR by removing the overlapping bony anatomy.

Bone-weighted Dual-energy Imaging

In this thesis, only soft-tissue weighted imaging was analyzed and optimized as our focus was its clinical application on lung SBRT patients. In the preliminary testing on the Rando phantom (Figure 34), bone-weighted DE imaging appeared promising, while the

soft-tissue weighted images were not working as intended, requiring optimization of the parameters.

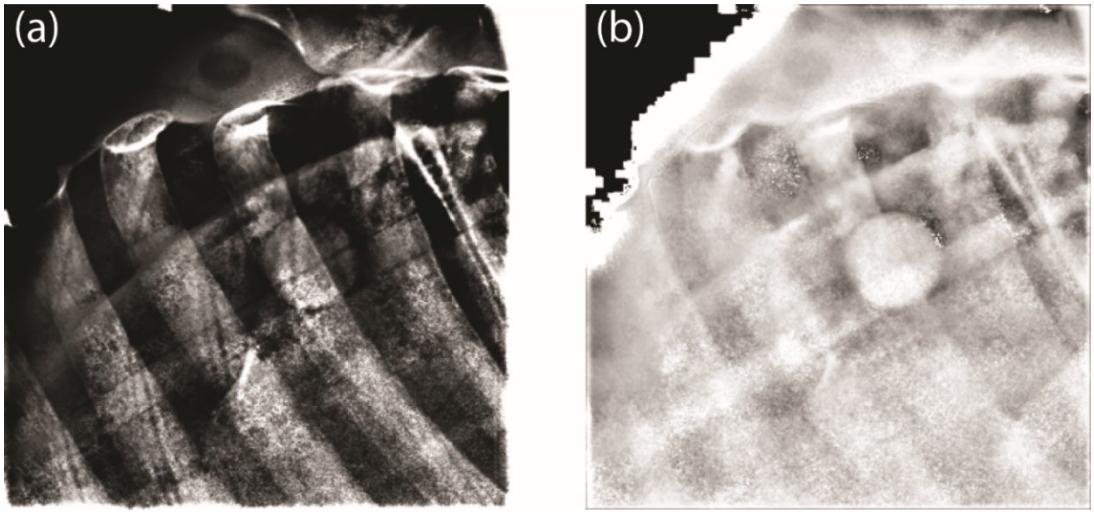

Figure 34 Preliminary results using the un-optimized DE images illustrating (a) the bone-weighted image and (b) the soft-tissue weighted image of the Rando phantom.

An optimized bone-weighted DE images is expected to improve DE image quality, and its clinical application would be for spine SBRT patients. Therefore, the most direct course for the future work would be to optimize bone-weighted DE imaging. A bone-weighted image is related to a soft-tissue weighted image, but it is complementary, i.e. rather than subtracting the LE image from the HE image, the opposite is carried out, as indicated by:

$$\ln(I_{DE}) = -\ln(I_{HE}) + w\ln(I_{LE})$$

While this algorithm is simple to achieve in the code that was written for the soft-tissue weighted images, a full optimization is warranted. This would include calculating the Energy Ratio from the previous chapter for the different tube potentials and thicknesses

of different materials. In calculating the ER, the spectrum should be weighted by a linear attenuation coefficient. In optimizing for soft-tissue weighted images, the bone linear attenuation coefficient is used for the scaling, since bone elimination was desired. For bone-weighted images, the soft-tissue linear attenuation coefficient would be used instead, slightly altering the results of the ER. Moreover, experimental data needs to be acquired with a physical phantom that represents spine SPRT patient geometry and a new cost function should be defined to maximize bone contrast while minimizing the soft tissue contrast. This physical phantom could be a modified version of the lung phantom, by adding a new spine layer to it. A non-optimized bone-weighted SLS image using the lung phantom is illustrated in Figure 35.

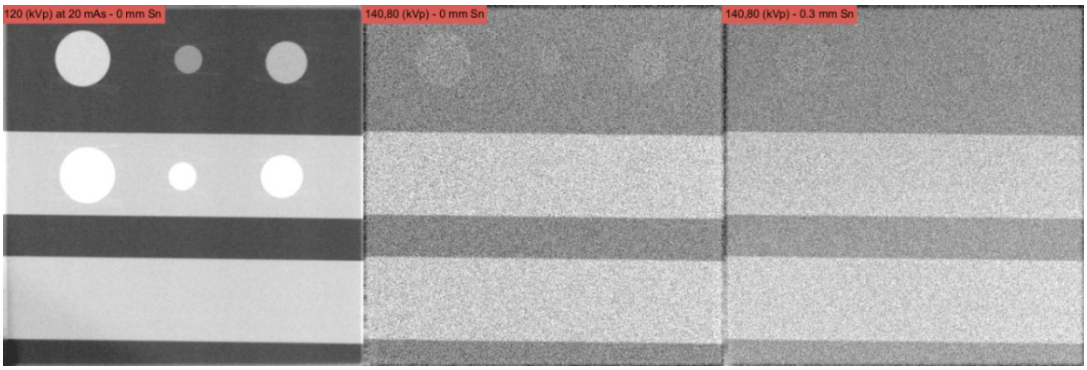

Figure 35 An illustration of a non-optimized bone-weighted SLS images from the lung phantom demonstrating a clinical SE image, a DE image with no filtration, and a DE image with 0.3 mm tin filtration.

The bone-weighted images in Figure 35 were obtained with the same setup as the soft-tissue weighted images, and the algorithms were not specifically designed for it. However, some features can still be noted on these non-optimized images, specifically

there is noticeable tumor elimination, while a marked bone contrast is still present. Noise would be further reduced with the ACNR algorithm that was implemented for the soft-tissue weighted images. Further improvements on the quality of the bone-weighted DE images can be expected if the parameters were optimized using both simulation and physical experiments.

Optimization of Dual-energy using Dual Filter

In this thesis, while a filter was examined for optimization, the same filter material and thickness was utilized for both the high and the low energy images. The intention was to eliminate any need for a mechanical switching device, which could potentially restrict fast kVp switching. However, the spectral separation could be augmented if different filters were used for the different energies. This includes a different filter material as well as a different filter thickness for each energy. The ER metric defined in the previous chapter could be used to optimize different filter materials and thicknesses. Figure 36 illustrates the ER values for different filter materials in the atomic number range 3 to 82 for each HE and LE beam.

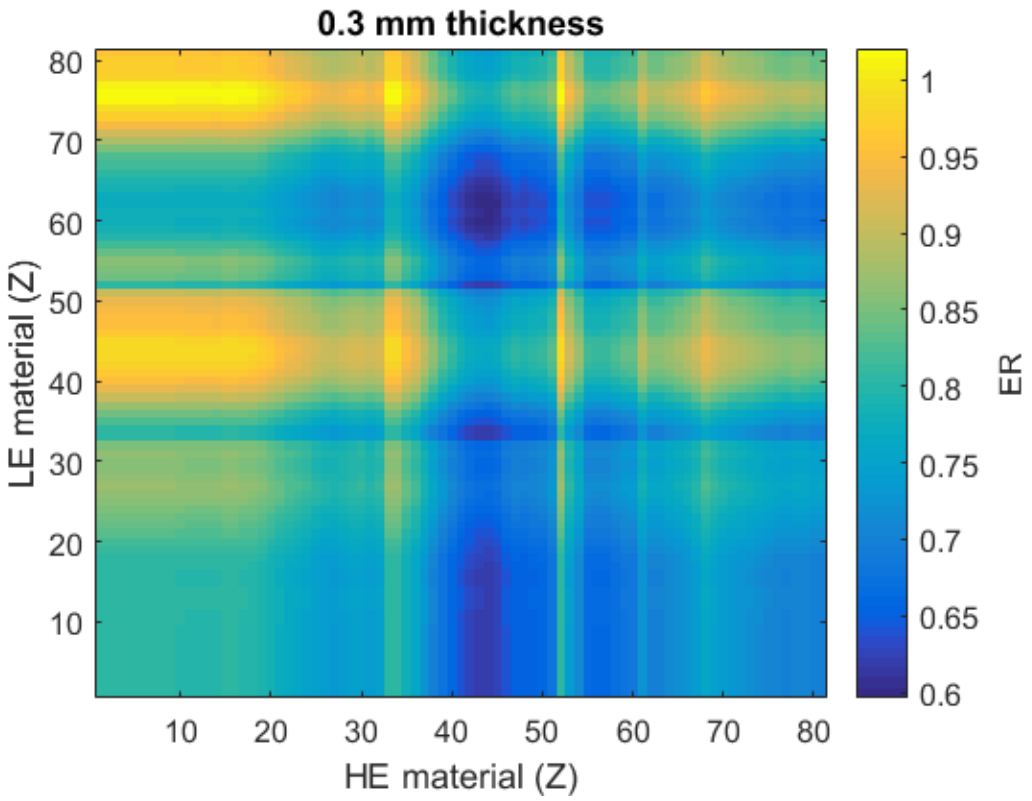

Figure 36 The Energy Ratio for a 0.3 mm thickness is illustrated for different filter materials for both the high energy (HE) and low energy (LE). A lower value of the ER enhances spectral separation.

As discussed in previous chapter, a lower ER value means increased spectra separation. The ER in Figure 36 was calculated for a fixed thickness of 0.3 mm of the filter material. This would need to be repeated for a range of thicknesses to create plots similar to what was carried out to find the trend for the same filter material in the previous chapter (Figure 27). A diagonal line along these plots corresponds to trends in Figure 27. If the trend stays the same over varying thicknesses, two different filter materials can be determined based on the overall trend of the ER. However, the ER is an idealized metric based solely on spectral separation. Therefore, it would not give full information about which thicknesses might yield enough detector signal to be clinically practical. Once the

materials are chosen for both high and low energies, experiments would have to be designed to identify the best combination of those filter thicknesses. This could be achieved with the current code that was used for this work. Using the cost function to evaluate the new filters, an optimal filter material and filter thickness combination could be achieved, using multiple filters for the different energies. A possible combination would be using materials that have a k-edge to achieve a distinctly separate low energy beam, while using a typical attenuator for the high energy beam. A K-edge material as a filter could possibly eliminate the need for two different energies, as the K-edge could lower the energy of the high energy beam into a low energy beam. To get a HE image, the filter would just need to be removed. Another option would be to just use a filter for the HE image, which would attenuate the low-energy portion of the spectrum, allowing for higher energy separation. Both of these methods rely on one filter for one of the energies, and no filter for the opposite energy. Either case would require a mechanical switch, as the filter would need to be removed or put in place for one of the energies. Once the cost function optimization is performed for soft-tissue weighted images, it would need to be repeated for bone-weighted images to investigate if results are different depending on what type of DE imaging is sought.

Dual-energy Imaging with Automatic Pixel-based Weighting Factor

DE imaging can be highly dependent on the weighting factor used for the logarithmic subtraction. If the proper weighting factor is not chosen, then the soft-tissue weighted DE image will not result in full bone elimination. To handle that problem, a cost function was

used to determine the weighting factor based on different ROIs. This approach determines the weighting factors quantitatively for the lung phantom with a fixed geometry used in previous chapter. However, for the Rando phantom, the weighting factors had to be determined manually by try and error since an ROI would not capture a unique tissue type in the projection image. An automated determination of the weighting factors for different patient geometry would be warranted in a clinical setting.

Moreover, another complicating factor is the dependence of the weighting factors on the thickness of the bone. A practical case is in chest imaging where both ribs and spine are in the field of view as illustrated in Figure 37. In this case, while one weighting factor is able to eliminate the ribs, the spine may still be present requiring a different weighting factor.

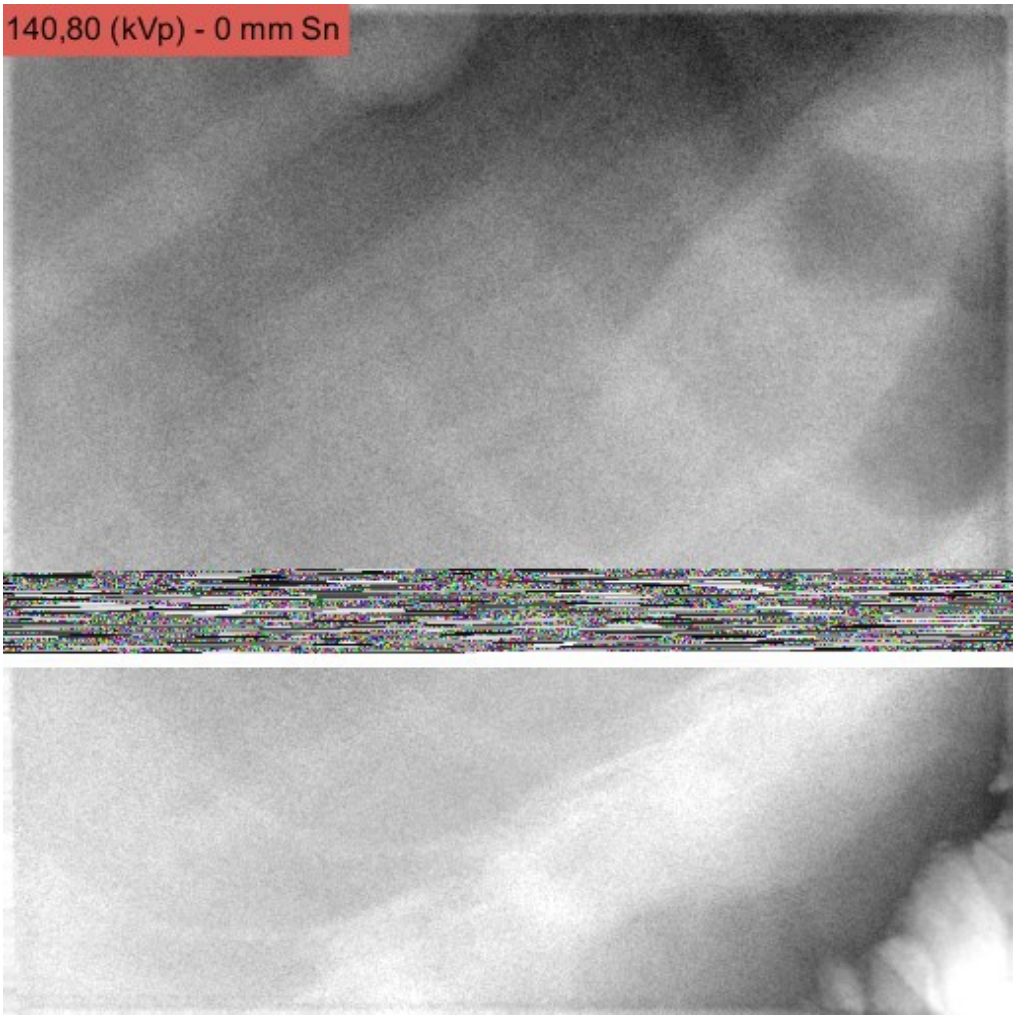

Figure 37 A DE image of the Rando phantom illustrating how some bones (e.g. ribs) are eliminated, while others, including the spine, are not for this weighting factor.

The ribs near the tumor have been eliminated, while the ribs closer to the spine, and the spine itself are not.

One solution to this problem would be to use *a priori* anatomical information from corresponding digitally remonstrated radiographs (DRR). Note that this information is only available for the radiotherapy patients but not for patients undergoing diagnostic radiography. This approach could allow for different weighting factors to be pre-

determined based on different regions and potentially for every pixel in the image. Thus the weighting factors would no longer be constants in the DE algorithm but rather an image itself. The weighting factor for every pixel would be dependent on the total thickness of the bone and soft tissue corresponding to the ray-line traced DRR pixel values. This approach could potentially allow for full bone elimination regardless of the angle or thickness of the bone or soft tissue anatomy. It could also allow for regions that have no bone overlap to be ignored by the algorithm, since those regions are already soft-tissue only. This would lower the additional noise in those regions that is gained by performing image subtraction.

Dual-energy Tumor Tracking for Lung SBRT Patients

Another future avenue to investigate is to design a stereoscopic DE system to track lung tumor motion in real-time for lung SBRT patients. To achieve this goal, first a soft-tissue weighted DE image would have to be designed as demonstrated in this thesis. However, the DE images would continuously be generated frame by frame as images are acquired. Then, a tracking algorithm should automatically identify the tumor in the DE image. Although this can be achieved with different techniques, the basic idea is to provide the algorithm a template of the tumor which can be derived from the soft-tissue-only DRRs, and the algorithm would then search the DE image and match the tumor template to the DE image by maximizing their cross correlation. The tumor would be identified in every frame allowing it to be tracked frame by frame in the software. A suitable candidate algorithm for both matching and tracking between frames is the shift invariant feature

transform (SIFT) [32]. The SIFT algorithm identifies distinct key points in the image to match to, then it not only performs the matching, but also follows those key points from frame to frame. As the algorithm follows the tumor, the treatment could then either be gated, or tracked. In the latter case, the treatment couch needs to adjust any shifts and/or the multi-leaf collimators (MLC) could track the tumor in real-time.

Final Remarks

This thesis demonstrated that dual-energy imaging is feasible on the ExacTrac stereoscopic imaging system without any modification to the current system. However, the results indicate that using 0.3 mm of tin filter for both the high and low energies produce noticeable bone elimination, tumor contrast, and noise reduction. This was achieved without additional imaging dose when compared to the clinical single energy imaging using current clinical protocol for a chest x-ray. The clinical implementation of this DE system could potentially allow for higher visibility of the tumor and higher accuracies in patient setup for lung SBRT. Currently, using the spine as a surrogate to align the patient is not reliable and thus physicians rely on CBCT. The use of DE could increase the accuracy of the ExacTrac imaging system by matching to soft-tissue instead of the spine. While this thesis has been focused on lung SBRT applications via obtaining DE soft-tissue weighted images, the research potential spans to a much broader horizon, including bone-weighted DE, dual filtering, automatic pixel-based weighting factor algorithm, and tumor tracking.

BIBLIOGRAPHY

[1] J. T. Bushberg and J. M. Boone, The essential physics of medical imaging, Lippincott Williams \& Wilkins, 2011.

[2] W. R. Hendee and E. R. Ritenour, Medical Imaging Physics, John Wiley & Sons, 2003.

[3] F. M. Khan, The Physics of Radiation Therapy, Lippincott Williams & Wilkins, 2003.

[4] C. Eriksson, "Optimization of Dual Energy data acquisition using CdTe-detectors with electronic spectrum splitting," 2013.

[5] W. A. Kalender, E. Klotz and L. Kostaridou, "An algorithm for noise suppression in dual energy CT material density images," *IEEE Transactions on Medical Imaging,* vol. 7, no. 3, pp. 218-224, 1988.

[6] D. L. Ergun, C. A. Mistretta, D. E. Brown, R. T. Bystrianyk, W. K. Sze, F. Kelcz and D. P. Naidich, "Single-exposure dual-energy computed radiography: improved detection and processing.," *Radiology,* vol. 174, no. 1, pp. 243-249, 1990.

[7] C. H. McCollough, M. S. Van Lysel, W. W. Peppler and C. A. Mistretta, "A correlated noise reduction algorithm for dual-energy digital subtraction angiography," *Medical physics,* vol. 16, no. 6, pp. 873-880, 1989.

[8] S. Richard and J. H. Siewerdsen, "Cascaded systems analysis of noise reduction algorithms in dual-energy imaging," *Medical physics,* vol. 35, no. 2, pp. 586-601, 2008.

[9] American Association of Physicists in Medicine, "Stereotactic body radiation therapy: The report of AAPM Task Group 101," Report no. 101, 2010.

[10] S. S. Lo, B. S. Teh, J. J. Lu and T. E. Schefter, Stereotactic Body Radiation Therapy, vol. 10, Springer Berlin Heidelberg, 2012, p. 978.

[11] R. D. Timmerman, B. D. Kavanagh, L. C. Cho, L. Papiez and L. Xing, "Stereotactic body radiation therapy in multiple organ sites," *Journal of Clinical Oncology,* vol. 25, no. 8, pp. 947-952, 2007.

[12] A. Ahmad and G. Shirish, Lung Cancer and Personalized Medicine, Springer International Publishing, 2016.

[13] R. L. Siegel, K. D. Miller and A. Jemal, "Cancer statistics, 2016," *CA: A Cancer Journal for*

Clinicians, vol. 66, no. 1, pp. 7-30, 2016.

[14] J. J. Sonke, M. Rossi, J. Wolthaus, M. van Herk, E. Damen and J. Belderbos, "Frameless stereotactic body radiotherapy for lung cancer using four-dimensional cone beam CT guidance," *International Journal of Radiation Oncology* Biology* Physics,* vol. 74, no. 2, pp. 567-574, 2009.

[15] N. A. Shkumat, J. H. Siewerdsen, A. C. Dhanantwari, D. B. Williams, S. Richard, N. S. Paul, J. Yorkston and R. van Metter, "Optimization of image acquisition techniques for dual-energy imaging of the chest," *Medical Physics,* vol. 34, no. 10, pp. 3904-3915, 2007.

[16] S. Richard and J. H. Siewerdsen, "Optimization of dual-energy imaging systems using generalized NEQ and imaging task," *Medical physics,* vol. 34, no. 1, pp. 127-139, 2007.

[17] A. N. Primak, J. R. Giraldo, X. Liu, L. Yu and C. H. McCollough, "Improved dual-energy material discrimination for dual-source CT by means of additional spectral filtration," *Medical physics,* vol. 36, no. 4, pp. 1359-1369, 2009.

[18] M. A. Hoggarth, J. Luce, F. Syeda, T. S. Bray, A. Block, S. Nagda and J. C. Roeske, "Dual energy imaging using a clinical on-board imaging system," *Physics in medicine and biology,* vol. 58, no. 12, p. 4331, 2013.

[19] T. Sherertz, M. Hoggarth, J. Luce, A. M. Block, S. Nagda, M. M. Harkenrider, B. Emami and J. C. Roeske, "Prospective evaluation of dual-energy imaging in patients undergoing image guided radiation therapy for lung cancer: Initial clinical results," *International Journal of Radiation Oncology* Biology* Physics,* vol. 89, no. 3, pp. 525-531, 2014.

[20] R. Patel, J. Panfil, M. Campana, A. M. Block, M. M. Harkenrider, M. Surucu and J. C. Roeske, "Markerless motion tracking of lung tumors using dual-energy fluoroscopy," *Medical physics,* vol. 42, no. 1, pp. 254-262, 2015.

[21] M. J. Menten, M. F. Fast, S. Nill and U. Oelfke, "Using dual-energy x-ray imaging to enhance automated lung tumor tracking during real-time adaptive radiotherapy," *Medical Physics,* vol. 42, no. 12, pp. 6987-6998, 2015.

[22] K. Matsumoto, M. Jinzaki, Y. Tanami, A. Ueno, M. Yamada and S. Kuribayashi, "Virtual monochromatic spectral imaging with fast kilovoltage switching: improved image quality as compared with that obtained with conventional 120-kVp CT," *Radiology,* vol. 259, no. 1, pp. 257-262, 2011.

[23] J. H. Siewerdsen, A. M. Waese, D. J. Moseley, S. Richard and D. A. Jaffray, "Spektr: A computational tool for x-ray spectral analysis and imaging system optimization," *Medical*

physics, vol. 31, no. 11, pp. 3057-3067, 2004.

[24] J. M. Boone and J. A. Seibert, "An accurate method for computer-generating tungsten anode x-ray spectra from 30 to 140 kV," *Medical physics,* vol. 24, no. 11, pp. 1661-1670, 1997.

[25] M. R. Ay, S. Sarkar, M. Shahriari, D. Sardari and H. Zaidi, "Assessment of different computational models for generation of x-ray spectra in diagnostic radiology and mammography," *Medical physics,* vol. 32, no. 6, pp. 1660-1675, 2005.

[26] American Association of Physicists in Medicine, "Standardized methods for measuring diagnostic x-ray exposure," Report no. 31, 1990.

[27] S. W. Alderson, L. H. Lanzl, M. Rollins and J. Spira, "An instrumented phantom system for analog computation of treatment plans.," *The American journal of roentgenology, radium therapy, and nuclear medicine,* vol. 87, pp. 185-195, 1962.

[28] American Association of Physicists in Medicine, "AAPM protocol for 40-300 kV x-ray beam dosimetry in radiotherapy and radiobiology," Report no. 61, 2001.

[29] M. T. R. Stevens, D. D. Parsons and J. L. Robar, "Continuous monitoring of prostate position using stereoscopic and monoscopic kV image guidance," *Medical Physics,* vol. 43, no. 5, pp. 2558-2568, 2016.

[30] American Association of Physicists in Medicine, "The management of imaging dose during image-guided radiotherapy: Report of the AAPM Task Group 75," Report no. 75, 2007.

[31] D. B. Williams, J. H. Siewerdsen, D. J. Tward, N. S. Paul, A. C. Dhanantwari, N. A. Shkumat, S. Richard, J. Yorkston and R. Van Metter, "Optimal kVp selection for dual-energy imaging of the chest: Evaluation by task-specific observer preference tests," *Medical physics,* vol. 34, no. 10, pp. 3916-3925, 2007.

[32] D. G. Lowe, "Distinctive image features from scale-invariant keypoints," *International journal of computer vision,* vol. 60, no. 2, pp. 91-110, 2004.

[33] H. E. Johns and J. R. Cunningham, The physics of radiology, Charles C. Thomas, 1983.